Zhuang *et al. Journal of Nanobiotechnology* (2025) 23:207
https://doi.org/10.1186/s12951-025-03281-6

Journal of Nanobiotechnology

RESEARCH **Open Access**

Harnessing the power of traceable system C-GAP: homologous-targeting to fire up T-cell immune responses with low-dose irradiation

Weijie Zhuang[1,2†], Kuangwu Pan[1,2,3†], Jie Wu[1,2†], Leyi Liu[1,2], Shiyu Lv[1,2], Jiajun Hu[1,2], Fangyang Shi[1,2], Wei Zhao[1,2*] and Dongsheng Yu[1,2*]

Abstract

While radiotherapy-induced immunogenic cell death (ICD) holds potential for enhancing cancer immunotherapy, the conventional high-dose irradiation often leads to an immunosuppressive microenvironment and systemic toxicity. Therefore, a biomimetic nanoplatform cell membrane coated-nitrogen-doped graphene quantum dots combined with Au nanoparticles (C-GAP) was developed in this study. Firstly, homologous and traceable targeting features of C-GAP enables tumor-selective accumulation, providing reference for the selection of the timing of radiotherapy. Secondly, radiosensitization by C-GAP with Low-dose irradiation (LDI) amplifies reactive oxygen species (ROS) generation to trigger potent ICD. Thirdly, remarkable immune remodeling induced by C-GAP enhances $CD8^+$T cell infiltration and effector function. Single-cell RNA sequencing revealed that C-GAP-LDI combination upregulates TNF and CCL signaling pathway expression in tumor-infiltrating $CD8^+$T cells which potentiates tumor eradication. Our findings present a novel approach for safe and effective radioimmunotherapy, where C-GAP sensitized LDI achieves therapeutic enhancement through precise ICD induction and systemic immune activation.

Keywords Biomimetic nanoparticle, Radioimmunotherapy, Immunogenic cell death (ICD), Homologous targeting, Oral squamous cell carcinoma (OSCC)

[†]Weijie Zhuang, Kuangwu Pan and Jie Wu contributed equally to this work.

*Correspondence:
Wei Zhao
zhaowei3@mail.sysu.edu.cn
Dongsheng Yu
yudsh@mail.sysu.edu.cn
Full list of author information is available at the end of the article

Graphical Abstract

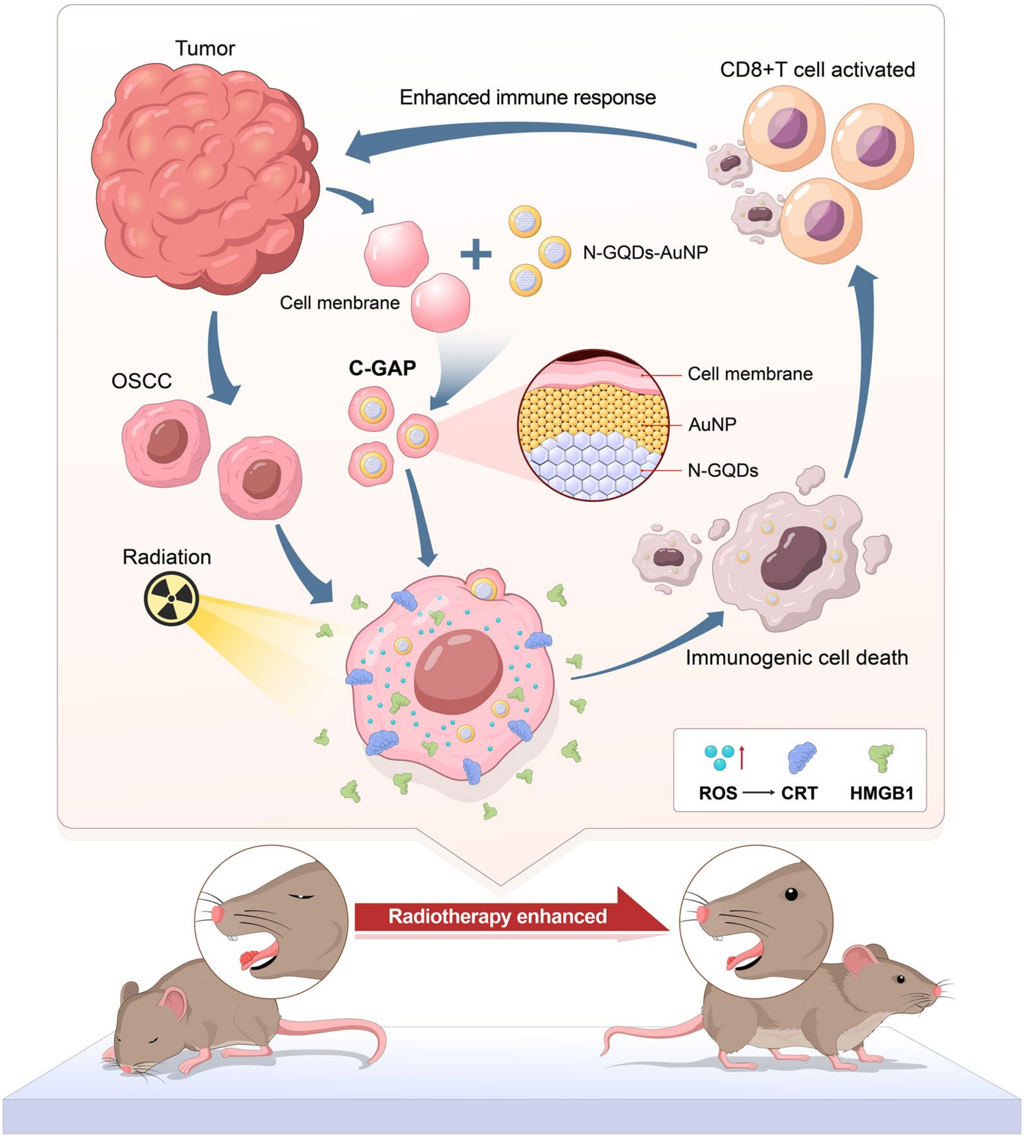

Background

Oral squamous cell carcinoma (OSCC) is one of the most common tumors in the head and neck region [1], with poor prognosis in late-stage patients, exhibiting a five-year survival rate of only 50–60% [2]. While immune checkpoint inhibitors have revolutionized cancer immunotherapy [3]. their efficacy in OSCC remains constrained by the immunosuppressive tumor microenvironment [4–6]. Enhancing the immunogenicity of the local tumor microenvironment and promoting the transition of the tumor immune microenvironment from "cold" to "hot" can help induce sustained and effective immune responses, potentially enhancing antitumor effects [7]. Radiotherapy, as a frontline treatment for OSCC, can effectively reduce the probability of tumor recurrence and metastasis [8–10]. Mechanistically, radiation-induced reactive oxygen species (ROS) provoke endoplasmic reticulum stress, autophagy, and apoptosis, culminating in immunogenic cell death (ICD) [11, 12]. This process releases damage-associated molecular patterns (DAMPs) that engage pattern recognition receptors (PRRs) on immune cells, enhancing tumor immunogenicity and establishing an "in situ vaccination" effect [13, 14]. Radiotherapy-induced ICD can mobilize and activate CD8 + T cells, further augmenting the effectiveness of immunotherapeutic interventions [15].

However, high-dose radiotherapy can cause vascular tissue damage, leading to local hypoxia in tumor tissues, reducing oxygen-dependent DNA damage [16], blocking the infiltration of $CD8^+$ T lymphocytes into tumors, and simultaneously recruiting immunosuppressive-related cells such as M2-like TAMs, MDSCs, CAFs, and Tregs, which reduce the sensitivity of tumor cells to radiotherapy and induce an immunosuppressive microenvironment [9, 17, 18]. This may be one of the main reasons for radiotherapy resistance. Additionally, high-dose radiotherapy can damage surrounding normal tissues, causing complications such as osteoradionecrosis of the jaw and radiation dermatitis, with significant systemic toxicity, limiting its clinical application.

Recent studies have shown that low-dose irradiation can downregulate the functions of immunosuppressive cells such as Tregs, M2-like TAMs, and tolerogenic DCs, recruit $CD8^+$ T cells and NK cells, effectively mobilize innate and adaptive tumor immunity, thereby reversing the tumor immunosuppressive microenvironment and enhancing tumor immune responses [19]. Nonetheless, low-dose irradiation exhibits an insufficiency in exerting a direct cytotoxic effect on tumor cells. The combination of radiotherapy with drugs or nanomaterials can effectively enhance the therapeutic efficacy against tumors. However, conventional treatment approaches, such as the combination of radiotherapy with chemotherapeutic drugs like cisplatin, are limited in their application due to issues like systemic toxicity and drug resistance [20, 21]. Therefore, the development of novel nanomaterials to precisely target tumor cells and sensitize them to low-dose irradiation, promoting ICD in tumor cells, may be a new entry point for radioimmunotherapy [22–24].

Graphene quantum dots (GQDs) are zero-dimensional nanomaterials based on graphene, possessing excellent biocompatibility and blood retention [25, 26]. As quantum dot materials, Nitrogen-Doped Graphene Quantum Dots (N-GQDs) exhibit unique photoluminescence properties [27], enabling the visualization of biodistribution and assisting in the precise and targeted control of drug delivery [25, 28–30]. Preliminary studies have shown that N-GQDs can effectively enhance the secretion of ROS to induce programmed cell death [31], suggesting its potential as the multifunctional drug carrier for radiosensitization. Gold nanoparticles/Au nanoparticles (AuNP), as nanomaterials with a high atomic number, can absorb, scatter, and emit radiation energy [32], while effectively modulating immune responses, inducing DC cell maturation, and increasing $CD8^+$ T cell activation and infiltration levels, serving as radiosensitizers with good immunomodulatory capabilities [33–35]. Therefore, combining N-GQDs with AuNP is expected to exert synergistic effects in radiosensitization and immunomodulation. Nanoparticles previously explored for radiotherapy sensitization, such as unmodified gold nanoparticles (GNPs), rely on the enhanced permeability and retention (EPR) effect to achieve passive tumor targeting. However, their limited bioavailability stems from insufficient systemic circulation time and inevitable phagocytosis by the reticuloendothelial system (RES). The lack of targeting specificity necessitates higher effective concentrations of GNPs to achieve therapeutic efficacy, which may exacerbate long-term toxicity and hinder clinical translation [36]. To address these challenges, advanced surface modifications or functionalization strategies are imperative to enhance tumor-targeting precision and optimize drug delivery efficiency [37]. Tumor cells can self-recognize and "home" to tumors through cell adhesion molecules (CAMs, such as EpCAM) and intercellular molecules (such as Galectin-3) on their cell membranes [38]. This special phenomenon in cancer cells is called "homologous adhesion" [39, 40]. Based on the mechanism of homologous adhesion, using tumor cell membranes to encapsulate nanomaterials can achieve homologous targeted delivery to tumor cells [38, 41–46].

In this study, based on the concept of homologous targeting, a biomimetic and visual drug delivery system was developed. Composite nanomaterials cell membrane coated-nitrogen-doped graphene quantum dots combined with Au nanoparticles (C-GAP) were synthesized by combining N-GQDs with AuNP and modifying it with OSCC cell membranes, which can exert radiosensitization and immune enhancement effects. Additionally, scRNA-seq was used to analyze its impact on $CD8^+$ effector T cells in the OSCC tumor immune microenvironment. The Graphical Abstract illustrates the construction of C-GAP and its mechanism of homologous targeted delivery to OSCC, sensitizing low-dose radiotherapy to induce ICD and regulating the immune microenvironment, ultimately potentiating the efficacy of radioimmunotherapy.

Materials and methods

Synthesis of N-GQDs, N-GQDs-AuNP, and C-GAP

Preparation of N-GQDs

N-GQDs were synthesized using a classic bottom-up hydrothermal method [47]. Initially, 1.0 g of dicyandiamide (DCD) and 2.0 g of citric acid (CA) were dissolved in 5.0 mL of distilled water. The solution was then transferred to a 25 mL Teflon-lined autoclave and reacted at 180 °C. The resultant product was dispersed in 100 mL of distilled water and centrifuged at 10,000 rpm for 10 min to collect the N-GQDs.

Synthesis of N-GQDs-AuNP

100 mg of N-GQDs were stirred and dissolved in 30 mL of ultrapure water to obtain an N-GQDs aqueous solution. Then, 2 mL of chloroauric acid (10 mM) was added and stirred for 30 min. The suspension was transferred to a covered glass bottle and heated at 50 °C for 4 h. The solution was dialyzed using a 1000D dialysis bag for 48 h and then dried at 80 °C to obtain N-GQDs-AuNP.

Extraction of cell membranes and preparation of C-GAP

Cell membranes were extracted from OSCC cells (SCC VII) using a membrane protein extraction kit (P0033, Beyotime) [41]. After digestion, cells were collected by centrifugation (1000 rpm, 5 min, 4 °C), washed and resuspended in PBS three times, and pretreated for 15 min on ice. Cells were lysed using a freeze–thaw method, and after centrifugation (700 g, 10 min, 4 °C), the supernatant was collected to remove cell nuclei. Further centrifugation (4 °C, 14000 g, 30 min) was performed to collect the cell membranes. N-GQDs-AuNP (1 mL, 2 mg/mL) were mixed with cell membranes (1 mL, 2 mg/mL) and stirred in an ice bath for 12 h. Excess cell membrane fragments were removed by centrifugation (6000 g, 10 min, 4 °C) to obtain C-GAP.

Characterization of N-GQDs, N-GQDs-AuNP, and C-GAP

Transmission electron microscopy (TEM) and energy dispersive spectroscopy (EDS) (Tecnai G2 Spirit T120 kV, Thermo) were used to observe the morphology, diameter, and analyze the elemental composition of the nanoparticles. Atomic force microscopy (AFM, Dimension Fastscan, Bruker) was employed to observe the surface morphology and particle size of the nanoparticles. Dynamic light scattering (NanoBrook Omni, Brookhaven Instruments Corporation) was used to determine the zeta potential of the nanoparticles. Raman spectroscopy (inVia Qontor, Renishaw), UV/Vis spectroscopy (Lambda 950, Perkin Elmer Limited), X-ray photoelectron spectroscopy (XPS, Nexsa, ThermoFisher), and Fourier transform infrared spectroscopy (FTIR, Vertex70-Hyperion3000, Bruker) were utilized to determine the functional groups and properties of the nanoparticles. A fluorescence spectrometer (FLS1000, Edinburgh Instruments) was used to measure the luminescence properties of the nanoparticles. Coomassie blue staining and Western blotting were employed to verify the composition of cell membrane proteins.

Cells and cell culture

SCC-VII cells were cultured in DMEM-F12 medium (GIBCO, C11330500BT) supplemented with 10% fetal bovine serum and 1% penicillin/streptomycin (GIBCO, A3160801) at 37 °C in a humidified incubator with 5% CO2. SCC-9 and SCC-15 cells were cultured in high-glucose DMEM medium (GIBCO, C11995500BT) with the same supplements.

Cell phagocytosis experiment

Equal numbers of SCC-VII, SCC-9, and SCC-15 cells were seeded onto confocal dishes and treated with C-GAP (10 μg/mL) overnight. The phagocytosis efficiency of the cells towards the material was detected by immunofluorescence staining under the confocal microscope (CLSM; LSM980, Zeiss), and the phagocytosis process of SCC-VII cells ingesting C-GAP was observed by TEM.

Western blotting

Cells treated with different conditions were collected by centrifugation and lysed on ice. After centrifugation (12000 g, 10 min) to remove cell debris, the lysates were mixed with 5×SDS sample buffer (P1040, Solarbio) and boiled for 10 min. Protein samples were separated by SDS-PAGE and transferred to PVDF membranes (ISEQ00010, Millipore). The membranes were blocked with 5% skimmed milk for 1 h and incubated with diluted primary antibodies Galectin-3 (WL03166, Wanleibio), Ep-CAM (WL01375, Wanleibio), HMGB1 (YT5502, Immunoway), CRT (YT0620, Immunoway), Na^+/K^+-ATPase (AF1864, Beyotime) overnight at 4 °C. After washing with TBST, the membranes were incubated with horseradish peroxidase-coupled secondary antibody buffer for 1 h at room temperature. Protein bands were detected using an affinity body ion ECL kit (KF001, Affinity Biosciences) on a chemiluminescence instrument (Clinx science, 3100Mini, 90,175).

ROS detection

Intracellular hydroxyl radical production was assessed using a DCFH-DA staining kit (S0033, Beyotime). After different treatments, cells were stained with DCFH-DA (10 μM) for 20 min. Cellular ROS levels were analyzed by flow cytometry (LSRFortessa, BD).

Immunofluorescence staining

SCC-VII cells were seeded onto confocal dishes and subjected to various treatments and cultures. After fixation with 4% paraformaldehyde, cells were blocked with 5% bovine serum albumin (BSA) for 30 min. Diluted primary antibodies against HMGB1 (YT5502, Immunoway) and CRT (YT0620, Immunoway) were added and incubated overnight at 4 °C. After washing with PBS, cells were incubated with fluorescent secondary antibodies for 1 h and washed again with PBS. Cell nuclei were stained with 4,6-diamidino-2-phenylindole (DAPI; 10 μg/mL) for 10 min, washed with

PBS, and mounted with an antifade reagent. Protein expression was observed using a laser confocal scanning microscope (CLSM; LSM980, Zeiss).

ATP detection

Intracellular ATP levels were detected using an ATP detection kit (S0026, Beyotime). SCC-VII cells were seeded into 6-well plates and subjected to different treatments and cultures. After lysis and centrifugation (4 °C, 12000 g, 5 min), the supernatant was collected. ATP assay working solution was added to 96-well plates, and 20μL of the sample was added after 5 min. RLU values were measured using a multifunctional microplate reader (Synergy H1, Biotek) and compared to a standard curve to calculate ATP concentrations.

Animal models

When tumor cells were cultured to sufficient quantities, they were washed twice with PBS, digested, neutralized, and centrifuged at 1000 rpm for 5 min. The supernatant was aspirated, and a cell suspension was prepared using serum- and antibiotic-free medium. Cell concentration was determined using a hemocytometer. The cell suspension was mixed with Matrigel (Corning, 354,234) and serum-free medium in a 1:3 ratio to achieve a concentration of 1×10^7/mL. A 1 mL syringe was used to inject 100μL of the tumor cell suspension subcutaneously into the left anterior tongue margin of C3H mice (Vital River Laboratory Animal Technology, Beijing, China). Tumors were visible on the tongue approximately 1–2 weeks after injection.

In vivo fluorescence distribution

To investigate the distribution and metabolism of C-GAP in mice, real-time fluorescence images of anesthetized C3H mice were captured at different time points (4, 12, and 24 h) using an in vivo imaging system (AniView Phoenix, BLT Photon Technology). Subsequently, their tumor tissues and major organs (heart, liver, spleen, lungs, and kidneys) were excised and imaged ex vivo. The average fluorescence intensity from the images was utilized to analyze the accumulation of nanoparticles in tumors and their biodistribution in major organs.

In vivo antitumor effect

After establishing the animal model of OSCC as previously described, mice were randomly divided into four groups of four mice each, totaling 16 mice, and treated as follows: ① intravenous injection of 200 μL PBS; ② intravenous injection of 200 μL of 1 μg/mL C-GAP; ③ intravenous injection of 200 μL PBS followed by radiation therapy with a 4 Gy dose of X-rays to the tumor tissue; ④ intravenous injection of 200 μL of 1 μg/mL C-GAP followed by localized radiation therapy with a 4 Gy dose of X-rays to the tumor tissue. PBS or C-GAP were injected on the first day. Mice in Groups ③ and ④ were anesthetized four hours post-injection, and radiation therapy was administered to the tumor site. Tumor size and mouse body weight were monitored every two days thereafter. Tumor length (a) and width (b) were measured using a vernier caliper, and tumor volume was calculated using the formula: Tumor Volume $(\mathrm{mm}^3) = a{*}b^2/2$. Mouse survival rates were monitored and recorded. For histopathological analysis, all mice were euthanized on Day 20 to collect tumor tissues and major organs (heart, liver, lungs, and kidneys). Tumor tissue weight was measured. Tumor tissues and major organs were fixed overnight in 4% paraformaldehyde solution, embedded in paraffin, and sectioned for H&E staining. Additionally, immunohistochemical staining (IHC) was performed to assess the proliferation index Ki67 (ab15580, Abcam), γ-H2AX (ET1602-2, Huabio), and HMGB1 (YT5502, Immunoway) in tumor tissues. Immunofluorescence staining was used to detect the expression of CD3e (DF6594, Affinity Bioscience) and CD8 (AF5126, Affinity Bioscience) in tumor tissues.

Single-cell RNA Sequencing (scRNA-seq)

After establishing the animal model of OSCC as previously described, mice were randomly divided into two groups, with three mice in each group, and subjected to the following treatments, respectively: (1)Control group: intravenous injection of 200 μL of phosphate-buffered saline (PBS); (2)Treatment group: intravenous injection of 200 μL of 1 μg/ml C-GAP followed by localized irradiation of the tumor tissue with a 4 Gy dose of X-rays for radiotherapy. PBS or C-GAP was injected on the first day after tumor establishment. Mice in Treatment group were anesthetized 4 h post-injection and irradiated at the site of tumor tissue formation. Seven days after treatment, the mice were euthanized, and tumor tissues were collected and processed into a single-cell suspension with a cell concentration of 700–1200 cells/μL. Each scRNA-seq sample was sequenced using the 10×Genomics system, and the raw data were processed with Cell Ranger (10×Genomics). The R (version 4.1.2), R Studio (version 1.3.1093) and the Seurat package (version 4.3.0) were used to read the scRNA-seq data files processed by 10×Genomics Cell Ranger. The DoubletFinder package (version 2.0.3) was utilized to identify and remove doublet cell data, followed by independent normalization of the scRNA-seq data for each sample using the Seurat package (version 4.3.0). Principal component analysis (PCA) was performed for dimensionality reduction, and Uniform Manifold Approximation and Projection (UMAP) was employed for nonlinear dimensionality reduction and visualization of the data. Cells were classified and annotated based on the gene expression profiles of known cell types in the database, followed by differential gene expression (DEG) analysis and Gene Ontology (GO) gene enrichment analysis.

Detailed experimental conditions (including C-GAP concentrations and radiation doses) for the aforementioned in vivo/in vitro experiments and scRNA-seq are provided in Supplementary Table S1.

Statistical analysis

Data analysis was conducted using GraphPad Prism 7.0, SPSS, and R-4.2.3 software. The statistical significance of differences among groups was evaluated using one-way ANOVA, two-way ANOVA, and the t-test. Results are expressed as the mean ± standard error of the mean (SEM) or standard deviation (SD), and statistical significance was determined at a significance level of $p < 0.05$.

Results and discussion

Synthesis and characterization of C-GAP

The preparation method of C-GAP is illustrated in Fig. 1A. After C-GAP was synthesized, TEM was used to scan the particle size and surface morphology of N-GQDs and N-GQDs-AuNP (Fig. 1B, C). N-GQDs with a diameter of approximately 3 nm and a uniform circular shape were observed [48, 49]. Additionally, gold nanoparticles bound to the surface of N-GQDs formed ellipsoid-like nanoparticles with a particle size of 20–30 nm, confirming the successful synthesis of N-GQDs-AuNP. Furthermore, AFM was employed to examine the surface morphology of N-GQDs-AuNP (Fig. 1D, E), revealing a nanoparticle surface thickness of approximately 30 nm, consistent with the observations from TEM. Subsequently, energy dispersive X-ray spectroscopy (EDS) was conducted for elemental analysis and verification (Fig. 1F). After eliminating the influence of the TEM supporting membrane (primarily composed of copper), it was found that N-GQDs-AuNP were composed of gold, carbon, nitrogen, and oxygen, validating the successful binding of N-GQDs with gold nanoparticles. Additionally, XPS was used to analyze the chemical composition of N-GQDs-AuNP (Fig. 1G, H and Fig. S1). Peaks at 287.52 eV, 398.70 eV, and 532.14 eV in NGQD corresponded to C1s, N1s, and O1s, respectively [50, 51]. In N-GQDs-AuNP, peaks at 86.94 eV, 285.13 eV, 398.95 eV, and 532.59 eV corresponded to Au4f, C1s, N1s, and O1s, respectively, demonstrating the successful reduction of gold nanoparticles on the surface of N-GQDs [51, 52].

Raman spectroscopy was further utilized to verify the structure of the graphene quantum dots in N-GQDs-AuNP [53]. Figure 2A displays the Raman spectrum of the composite nanomaterial N-GQDs-AuNP, showing two representative peaks at 1335.34 cm^{-1} and 1576.6 cm^{-1} corresponding to the classic D-band (ID) and G-band (IG) of graphene quantum dots, respectively [53]. The D-band arises from defects in the graphene structure, while the G-band is due to the tangential C–C bond vibrations [54].

Figure 2B presents the UV–Vis absorption spectrum of N-GQDs-AuNP. It can be observed that N-GQDs exhibit a strong absorption peak at 231 nm, which may be related to the $n \rightarrow \pi$ and $n \rightarrow \pi^*$ transition of C = C double bonds [55, 56]. In contrast, HAuCl4 solution shows strong absorption peaks at both 220 nm and 290 nm. N-GQDs-AuNP combines the characteristics of both, with a strong absorption peak at 231 nm and a weaker one at 297 nm.

Graphene quantum dots possess excellent luminescent properties [57], and nanomaterials developed based on them are widely used in bioimaging and drug delivery [58]. We employed photoluminescence spectroscopy (PL spectroscopy) to verify the luminescent properties of N-GQDs and the composite nanomaterial N-GQDs-AuNP [59]. Figure 2C, D demonstrate that under excitation light at a wavelength of 360 nm, both N-GQDs and N-GQDs-AuNP exhibit good luminescent properties, with emission peaks located at 425 nm and 434 nm, respectively.

Next, FTIR was used to verify the surface functional group structure of N-GQDs and N-GQDs-AuNP. As shown in Fig. 2E, in NGQD, the peak at 3137 cm^{-1} is mainly associated with the stretching vibrations of hydroxyl O–H bonds and amine N–H groups. The peaks at 1639 cm^{-1} and 1429 cm^{-1} may be attributed to C = O double bonds or C = C double bonds and CH2 bonds, respectively [55, 60–63]. After binding with gold nanoparticles, the peaks on N-GQDs-AuNP changed. The peak at 3334 cm^{-1} may be due to the reduction of $Au3^+$ ions by aldehydes/ketones/hydroxyaldehydes on the surface of N-GQDs, generating more -OH termini and resulting in a blue shift of this peak [64]. The peaks at 1619 cm^{-1} and 1342 cm^{-1} may be related to changes in the vibration modes of C = O double bonds or C = C double bonds and CH2 bonds, respectively[65].

Furthermore, the ZETA potential of N-GQDs-AuNP was measured to be -38.1 mV using a laser particle size analyzer (Fig. 2F). After successfully modifying N-GQDs-AuNP with OSCC SCC-VII cell membranes to synthesize C-GAP, we observed through TEM that the surface of C-GAP was coated with cell membranes (Fig. 2G). Coomassie blue staining (Fig. 2H) was used to detect the proteins contained in C-GAP, and it was found that the protein profile was similar to that expressed by

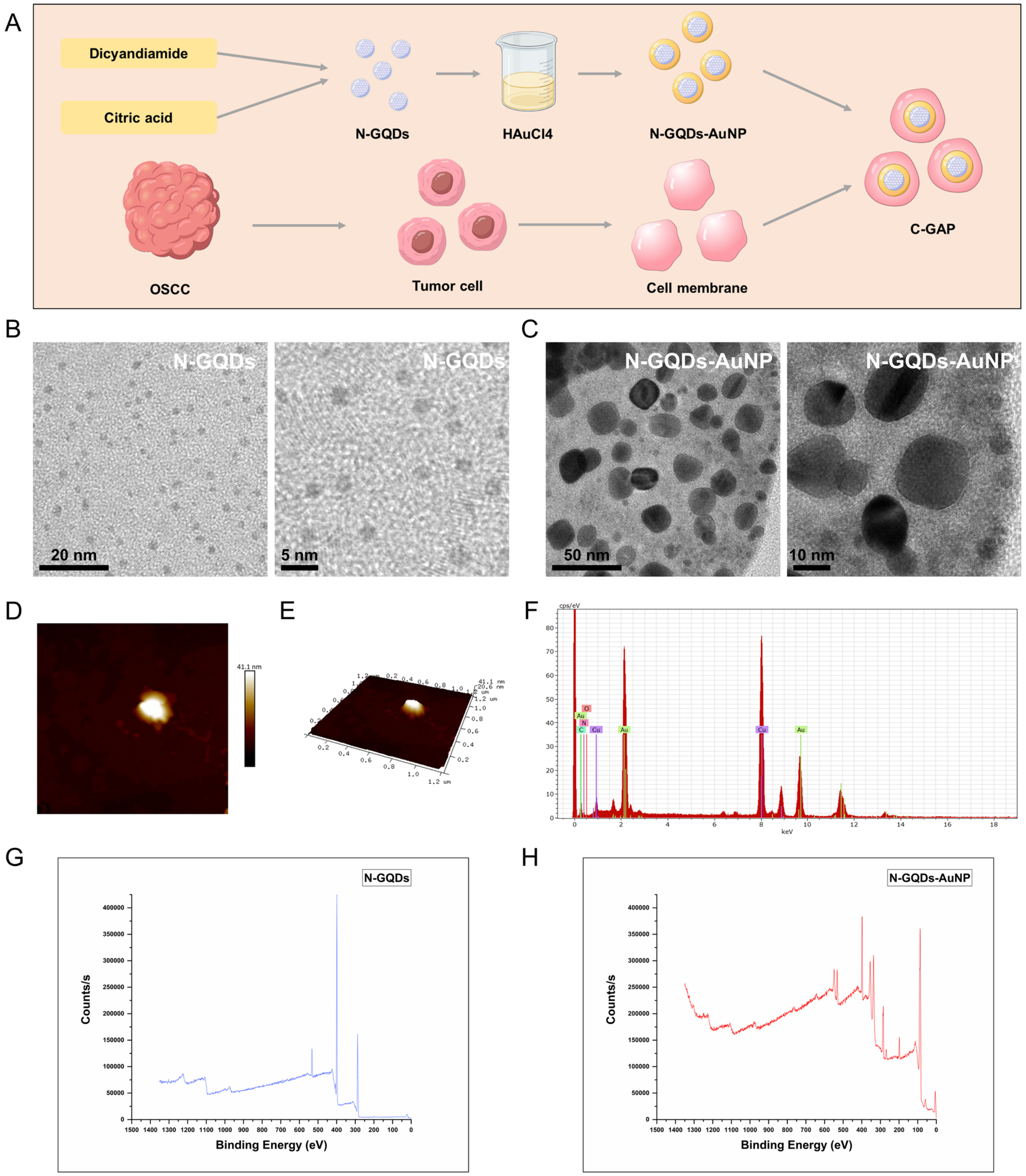

Fig. 1 Synthesis and Characterization of C-GAP. **A** Schematic Diagram of the Synthesis of C-GAP. **B**, **C** Morphology and Particle Size of N-GQDs and N-GQDs-AuNP Observed under TEM. **D-E** Surface Morphology of N-GQDs-AuNP Detected by AFM. **F** Elemental Composition of N-GQDs-AuNP Analyzed by Energy-Dispersive X-ray Spectroscopy (EDS). **G**, **H** Chemical Structure of N-GQDs and N-GQDs-AuNP Analyzed by X-ray Photoelectron Spectroscopy (XPS)

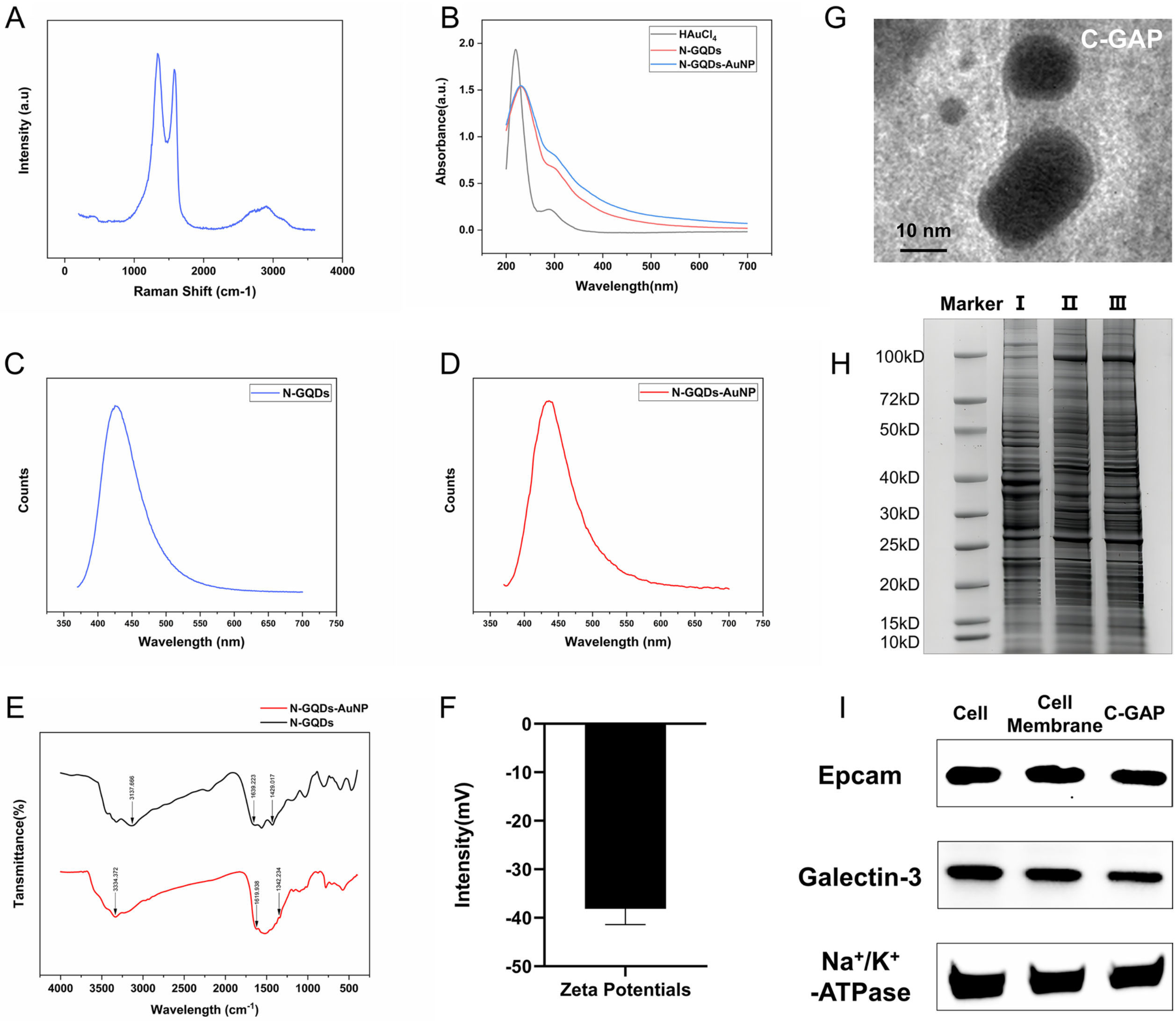

Fig. 2 Characterization Experiments of C-GAP. **A** Raman Spectroscopy for Chemical Structure Analysis of N-GQDs-AuNP. **B** UV–Visible Spectroscopy for Characteristic Peak Detection of N-GQDs-AuNP. **C-D** Photoluminescence (PL) Spectroscopy for Evaluating the Photoluminescent Properties of N-GQDs and N-GQDs-AuNP. **E** Fourier Transform Infrared (FTIR) Spectroscopy for Functional Group Analysis of N-GQDs and N-GQDs-AuNP. **F** Dynamic Light Scattering (DLS) for Zeta Potential Measurement of N-GQDs-AuNP (n = 3). **G** Morphology and Particle Size Observation of C-GAP under TEM. **H** Coomassie Blue Staining for Protein Distribution Detection on the Surface Membrane of C-GAP. **I** Representative Images of Western Blotting for Expression Analysis of Cell Adhesion Molecule EpCAM and Intercellular Molecule Galectin-3 on the Surface Membrane of C-GAP (n = 3). The data are presented as the means ± SDs. ns $P > 0.05$, *$P < 0.05$, **$P < 0.01$, ***$P < 0.001$

the cell membranes. Western blotting results (Fig. 2I) indicated that the surface of C-GAP contained the cell adhesion molecule EpCAM and the intercellular molecule Galectin-3[39], confirming successful coating and modification of the material with cell membranes. In summary, the above experimental results validate the successful synthesis of C-GAP.

In vitro cellular phagocytosis experiments of C-GAP

Encapsulating nanoparticles with tumor cell membranes based on the homologous adhesion mechanism can impart better biocompatibility and lower immunogenicity to the nanoparticles [38]. Through the binding of CAMs and intercellular molecules, tumor homologous targeting can be achieved, thereby enabling the nanoparticles to deeply penetrate tumor cells and contributing to precise tumor treatment [38]. The strategy of utilizing cell membrane-modified nanomaterials

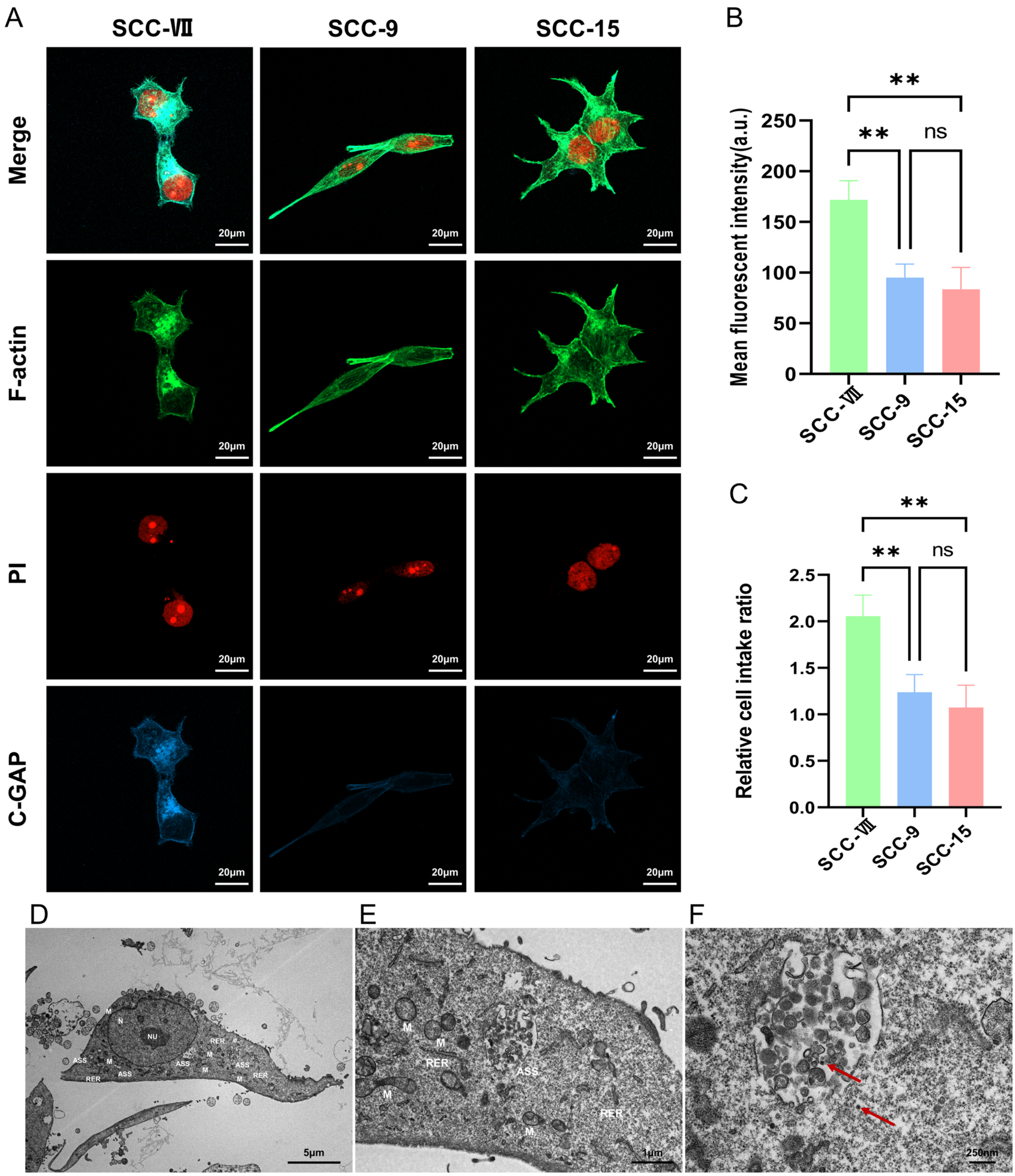

Fig. 3 In Vitro Cellular Phagocytosis Experiment of C-GAP. **A** Representative Images of C-GAP Internalization by SCC-VII, SCC-9, and SCC-15 Cells Detected by Immunofluorescence Staining. **B**, **C** Semi-Quantitative Analysis of C-GAP Internalization Efficiency by SCC-VII, SCC-9, and SCC-15 Cells (n = 5, one-way ANOVA test). **D**–**F** Observation of C-GAP Internalization Process by SCC-VII Cells under TEM, Highlighting Cellular Structures Including Nucleus (N), Nucleolus (NU), Mitochondria (M), Rough Endoplasmic Reticulum (RER), and Autophagolysosome (ASS), with Red Arrows Indicating C-GAP After Cellular Phagocytosis. The data are presented as the means ± SDs. ns $P > 0.05$, *$P < 0.05$, **$P < 0.01$, ***$P < 0.001$

has been applied in the treatment of various epithelial-derived malignancies, including breast cancer and colon cancer [66]. We validated the tumor targeting ability of C-GAP by incubating it with different types of OSCC cells (SCC-VII, SCC-9, SCC-15) and utilizing the luminescent visualization property of C-GAP along with immunofluorescence staining. Confocal imaging results and semi-quantitative analyses (Fig. 3A–C) revealed that, compared to other OSCC cell lines, the SCC-VII cell line exhibited higher specific recognition and uptake rates for C-GAP modified with SCC-VII cell membranes, with statistically significant differences ($p < 0.01$). Additionally, the uptake process of C-GAP by SCC-VII cells was observed through TEM (Fig. 3D–F). These results indicate that tumor cell membrane modification can enhance the specific uptake of nanomaterials by tumor cells, and C-GAP possesses excellent tumor homologous targeting and homing abilities, enabling precise drug delivery. Notably, given the ubiquitous expression of CAMs (e.g., EpCAM) and intercellular molecules (e.g., Galectin-3) across various epithelial cancers, the targeted delivery of C-GAP nanoparticles could theoretically be generalized to other tumor through engineering modifications involving tumor cell membrane coating [40, 67, 68].

In vitro biocompatibility and radiosensitization effects of C-GAP for radiotherapy

The cytotoxicity of C-GAP was tested using live/dead cell staining (Fig. 4A, B and Fig. S2). The experimental results showed that C-GAP at concentrations of 1 μg/ml or below had no significant impact on the growth of the OSCC cell line SCC-VII. At a concentration of 5 μg/ml, it had a slight effect on cell growth, while at concentrations of 10 μg/ml or above, it exhibited significant cytotoxicity. The CCK-8 assay (Fig. 4C) and Cell Cloning Formation test (Fig. 4D, E) further confirmed the biocompatibility of C-GAP. Therefore, a concentration of 1 μg/ml was selected for subsequent C-GAP radiosensitization experiments. Radiotherapy with doses less than 5 Gy can reverse the tumor immunosuppressive microenvironment, and radiosensitization through low-dose radiotherapy can enhance tumor killing while boosting immunity, exerting a synergistic effect [19, 69].

Next, in vitro cell irradiation experiments were conducted to test the radiosensitization effect of C-GAP on tumor cell killing by low-dose radiotherapy. SCC-VII cells were co-incubated with 1 μg/ml of C-GAP for 24 h and then irradiated with different doses for another 24 h. Live/dead cell fluorescent staining (Fig. 4F–H and Fig. S3), CCK-8 assay (Fig. 4I), and Cell Cloning Formation test (Fig. 4J, K) were used to verify that C-GAP combined with radiotherapy at doses above 4 Gy could achieve the best tumor killing effect. The above results indicate that C-GAP has good radiosensitization properties and, in combination with low-dose radiotherapy of 4 Gy, can exert an ideal tumor killing effect.

Induction of ICD in OSCC cells by C-GAP

Radiotherapy can upregulate the levels of ROS and ATP in tumor cells, enhance the expression of ICD-related molecules such as HMGB1 and CRT, induce ICD in tumor cells, and thereby increase tumor immunogenicity, achieving a "tumor in situ vaccination effect" [70, 71]. Immunofluorescence staining combined with confocal microscopy revealed that compared to the Control group and the C-GAP group (Fig. 5), the Radiation group significantly increased the expression of HMGB1 and CRT in tumor cells, while the C-GAP + Radiation group further enhanced the expression of HMGB1 and CRT compared to the Radiation group, as shown in Fig. 6A–D. Subsequent Western blotting results (Fig. 6E) confirmed the upregulation of HMGB1 and CRT expression in the Radiation group and further upregulation in the C-GAP + Radiation group. Flow cytometry results (Fig. 6F) showed a significant upregulation of ROS levels in tumor cells in the C-GAP + Radiation group. ATP levels in the cells were detected using an ATP detection kit and a microplate reader. As shown in Fig. 6G, the Radiation group exhibited significantly elevated ATP levels compared to the Control group and the C-GAP group, while the C-GAP + Radiation group had the highest ATP expression levels. These results indicate that C-GAP radiosensitization with low-dose radiotherapy can significantly promote ICD in tumor cells, further enhancing tumor immunity.

In vivo distribution, biocompatibility, and antitumor effect of C-GAP

Benefiting from its excellent photostability and multifunctional photoluminescent properties, nanomaterials developed based on graphene quantum dots are often applied in biological imaging fields such as targeted and visual drug delivery[72]. Based on in vitro cellular validation, the biodistribution of C-GAP in mice was further detected through in vivo imaging techniques (Fig. 6A). In vivo fluorescence imaging of mice was performed at 4, 12, and 24 h after tail vein injection of C-GAP. At 4 h post-injection, it was observed that C-GAP was specifically taken up by tumor tissue compared to other tissues and organs, validating the exceptional tumor-targeting ability of C-GAP. Comparing

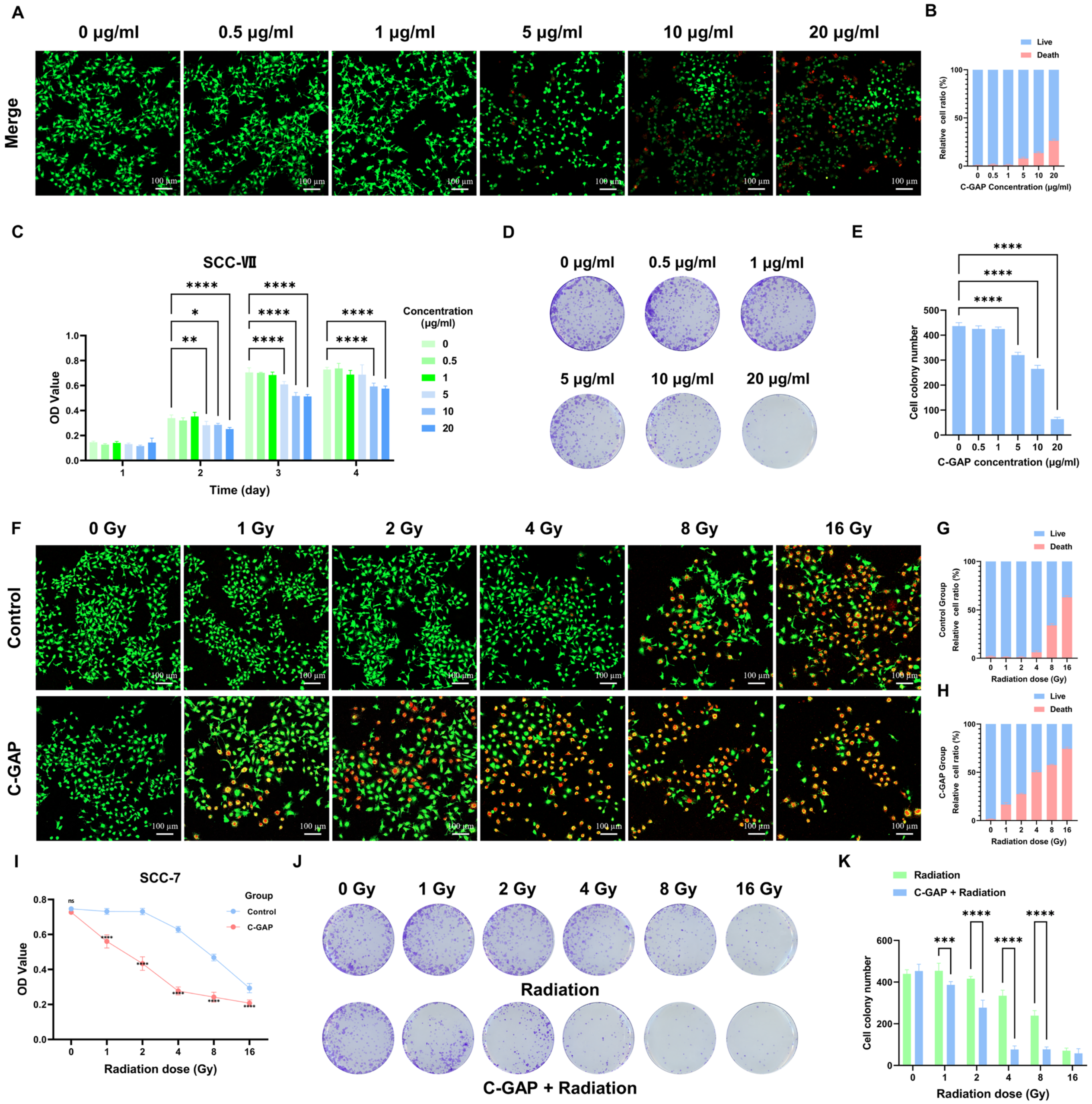

Fig. 4 In Vitro Biocompatibility of C-GAP and Its Enhancement of Radiotherapy Efficacy. **A**, **B** Representative Images and Semi-Quantitative Analysis of Cytotoxicity of 0–20 μg/ml C-GAP on SCC-VII Cells Observed under Confocal Microscopy After Live/Dead Cell Staining (n = 5, one-way ANOVA test, green fluorescence represents SYTO9 for live cells, red fluorescence represents PI for dead cells). **C** CCK-8 Assay to Assess the Effect of 0–20 μg/ml C-GAP on the Proliferation Activity of SCC-VII Cells (n = 5, one-way ANOVA test). **D**–**E** Representative Images and Semi-Quantitative Analysis of the Impact of 0–20 μg/ml C-GAP on the Growth of SCC-VII Cells Using the Cell Cloning Formation Test (n = 5, one-way ANOVA test). **F**–**H** Representative Images and Semi-Quantitative Analysis of the Killing Effect of 1 μg/ml C-GAP Combined with 0–16 Gy Radiotherapy on SCC-VII Cells Observed under Confocal Microscopy After Live/Dead Cell Staining (n = 5, one-way ANOVA test, green fluorescence represents SYTO9 for live cells, red fluorescence represents PI for dead cells). **I** CCK-8 Assay to Evaluate the Effect of 1 μg/ml C-GAP Combined with 0–16 Gy Radiotherapy on the Proliferation Activity of SCC-VII Cells (n = 5, one-way ANOVA test). **J-K** Representative Images and Semi-Quantitative Analysis of the Impact of 1 μg/ml C-GAP Combined with 0–16 Gy Radiotherapy on the Growth of SCC-VII Cells Using the Cell Cloning Formation Test (n = 5, t-test). The data are presented as the means ± SDs. ns $P > 0.05$, *$P < 0.05$, **$P < 0.01$, ***$P < 0.001$

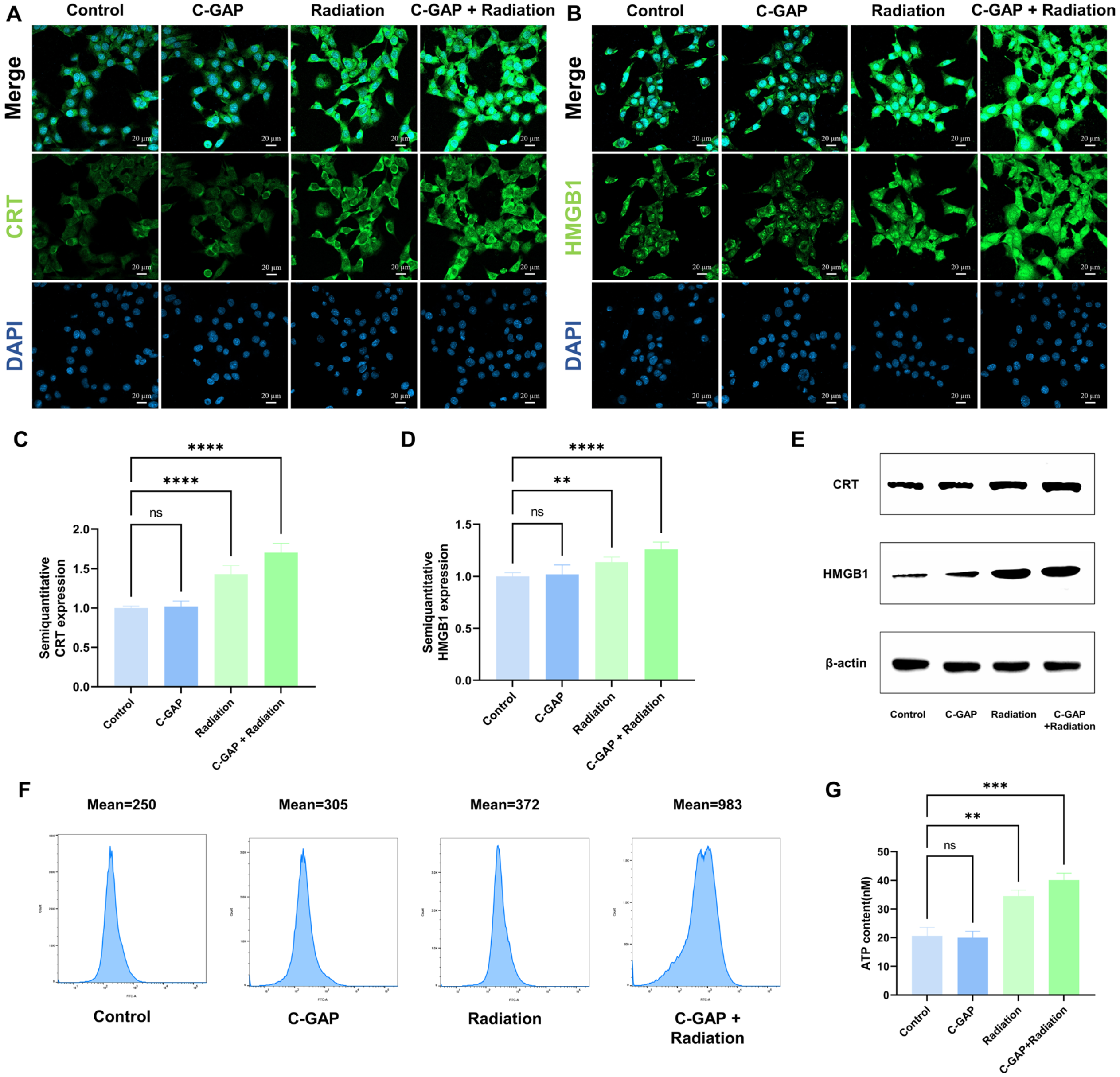

Fig. 5 In Vitro Experiments on C-GAP-Induced ICD in OSCC Cells. **A**–**D** Representative Images and Semi-Quantitative Analysis of CRT and HMGB1 Expression in SCC-VII Cells from Different Groups Detected by Immunofluorescence Staining (n = 5, one-way ANOVA test). **E** Representative Images of Western Blotting Analysis of CRT and HMGB1 Expression in SCC-VII Cells from Different Groups (n = 5). **F** Flow Cytometry Detection of ROS Levels in SCC-VII Cells from Different Groups. **G** Microplate Reader Measurement of ATP Levels in SCC-VII Cells from Different Groups (n = 5, one-way ANOVA test). The data are presented as the means ± SDs. ns $P > 0.05$, *$P < 0.05$, **$P < 0.01$, ***$P < 0.001$

(See figure on next page.)

Fig. 6 In Vivo Experiments on Bioimaging, Biocompatibility, and Antitumor Effects of C-GAP. **A**–**C** Live Imaging and Quantitative Analysis of C-GAP Distribution in Various Organs after Tail Vein Injection in C3H Mice. **D**–**F** Comparison of Tumor Weight, Tumor Volume Changes, and Body Weight Changes in C3H Mice from Different Groups (n = 4, one-way ANOVA test). **G** Physical Images of Tumor Size in C3H Mice from Different Groups (n = 4, one-way ANOVA test). **H** Representative Images of H&E Staining of Tumor Tissue from C3H Mice in Different Groups (n = 4, one-way ANOVA test). **I** Representative Images of Immunohistochemical Staining for Ki67 in Tumor Tissue from C3H Mice in Different Groups (n = 4). The data are presented as the means ± SDs. ns $P > 0.05$, *$P < 0.05$, **$P < 0.01$, ***$P < 0.001$, ****$P < 0.0001$

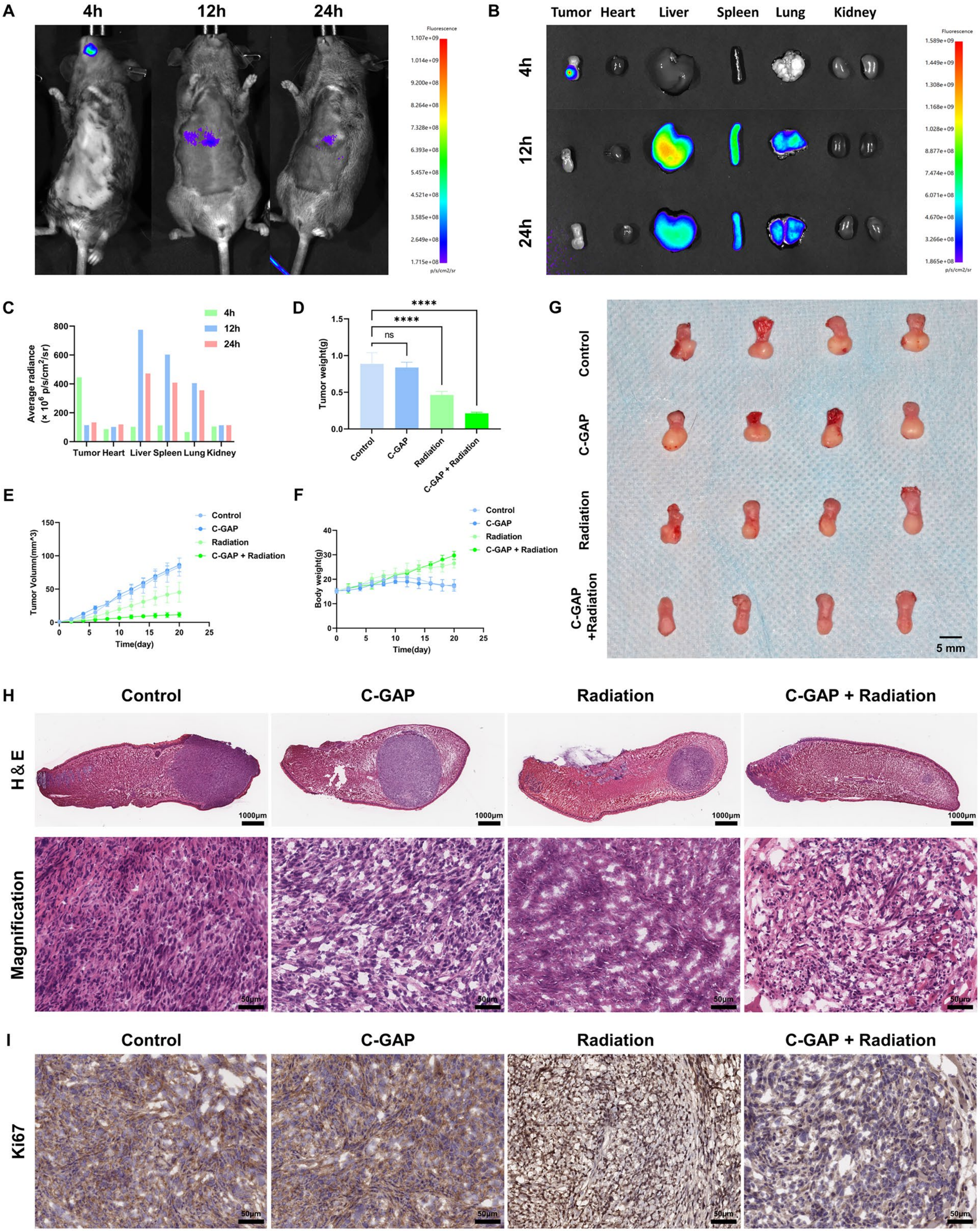

Fig. 6 (See legend on previous page.)

the results at 4, 12, and 24 h (Fig. 6B, C), it was found that the fluorescence signals in the liver, spleen, and lungs first increased and then gradually decreased, indicating that C-GAP may accumulate in the spleen through pulmonary blood circulation to activate immune responses and finally undergo metabolism through the liver.

To verify the radiosensitization effect of C-GAP on tumors in vivo, C3H OSCC mice were randomly divided into four groups: Control, C-GAP, Radiation, and C-GAP + Radiation. After different treatments for each group, the mice's body weight and tumor growth were monitored every two days. All mice were euthanized on day 20, and their tumor weights were measured. Figure 6D shows that the C-GAP + Radiation group had the lowest tumor weight, followed by the Radiation group, while the C-GAP and Control groups had no significant difference and exhibited the largest tumor weights. Figure 6E demonstrates that the tumor volume gradually increased in the Control group during the experiment, with no significant difference in tumor volume change between the C-GAP group and the Control group. The tumor volume growth was slower in the Radiation group, while it was significantly smaller in the C-GAP + Radiation group. Figure 6F indicates that the mouse body weights gradually increased in the Radiation and C-GAP + Radiation groups during the experiment. However, due to the impact of tongue tumors on feeding, the mice in the Control and C-GAP groups developed cachexia in the later stages of the experiment, with their body weights gradually decreasing after a slight increase. The final tumor morphologies are shown in Fig. 6G. Further H&E and ki67 staining of tumor tissue sections were performed to assess the therapeutic effect (Fig. 6H, I). Ki67 staining results showed that tumor cell proliferation was significantly reduced in the C-GAP + Radiation group, followed by the Radiation group, while there was no significant difference between the C-GAP and Control groups. Additionally, H&E staining results of vital organs (heart, liver, lungs, and kidneys) further validated that C-GAP had no significant cytotoxicity (Fig. S4). These experimental results demonstrate that C-GAP has good biocompatibility, can target and deliver drugs to tumors precisely through visualization, and significantly inhibits tumor tissue growth by radiosensitization.

In vivo experiments on C-GAP-induced ICD in tumors

Immunohistochemical staining for γ-H2AX was performed to verify the ability of C-GAP-sensitized radiotherapy to induce DNA damage in tumor cells. As shown in Fig. 7A, the highest levels of γ-H2AX were observed in the C-GAP + Radiation group, followed by the Radiation group, indicating that C-GAP-sensitized radiotherapy can induce DNA damage leading to cell death. Further immunohistochemical detection of the expression of HMGB1, a marker associated with ICD, in tumor tissues was conducted. The results in Fig. 7B showed high expression of HMGB1 in both the Radiation and C-GAP + Radiation groups. Additionally, immunofluorescence was used to detect the infiltration levels of $CD3^+CD8^+$ T cells in mouse tumor tissues (Fig. 7C). The results demonstrated that the infiltration levels of $CD3^+CD8^+$ T cells were significantly increased in the C-GAP + Radiation group compared to the Control group. These findings suggest that C-GAP combined with low-dose radiotherapy can induce ICD in tumor cells and further increase the infiltration levels of $CD3^+CD8^+$ T cells in the tumor immune microenvironment.

scRNA-seq analysis of C-GAP's regulatory role in the tumor immune microenvironment

Despite the development of various radiosensitizers in previous studies, there remains a lack of targeted research analyzing the impact of nanomaterials as radiosensitizers for low-dose radiotherapy on immune effector cells within the tumor immune microenvironment. Previous in vitro and in vivo experiments have validated C-GAP as an effective radiosensitizer and ICD inducer, exerting synergistic effects on radiosensitization and immune regulation. To further investigate the regulatory role and potential mechanisms of C-GAP combined with low-dose radiotherapy on tumor immune effector cells, we conducted scRNA-seq on untreated tumor tissues from the Control group and tumor tissues from the Treatment group. We analyzed the composition and gene expression differences of $CD8^+$ T cells in the tumor tissues, with the workflow outlined in Fig. 8A. Based on cell surface markers, $CD8^+$ T cells were initially classified into 13 subpopulations (Fig. 8B). Further analysis was then conducted on the expression of 15 $CD8^+$ T cell-specific marker molecules across these 13 subpopulations, as shown in Fig. 8C, D. According to the expression patterns of these 15 marker molecules, $CD8^+$ T cells were further categorized into five major classes: Exhausted T cells, Proliferation T cells, Pre-Exhausted T cells, Effector T cells, and Naive/Memory T cells, as illustrated in Fig. 8E. A comparative analysis of the number, composition, and proportions of effector T cells between the Control and Treatment groups was conducted (Fig. 8F, G). The results showed that, compared to the control group, the overall number of $CD8^+$ T cells significantly increased in the Treatment group (from 1452 to 5292). Specifically, the proportion of Naive/Memory T cells significantly rose (from 19.21% to 46.81%, $p = 0.0067 < 0.05$), while the proportion of Exhausted T cells significantly decreased (from 23.35% to 6.48%, $p = 0.04 < 0.05$). The proportion

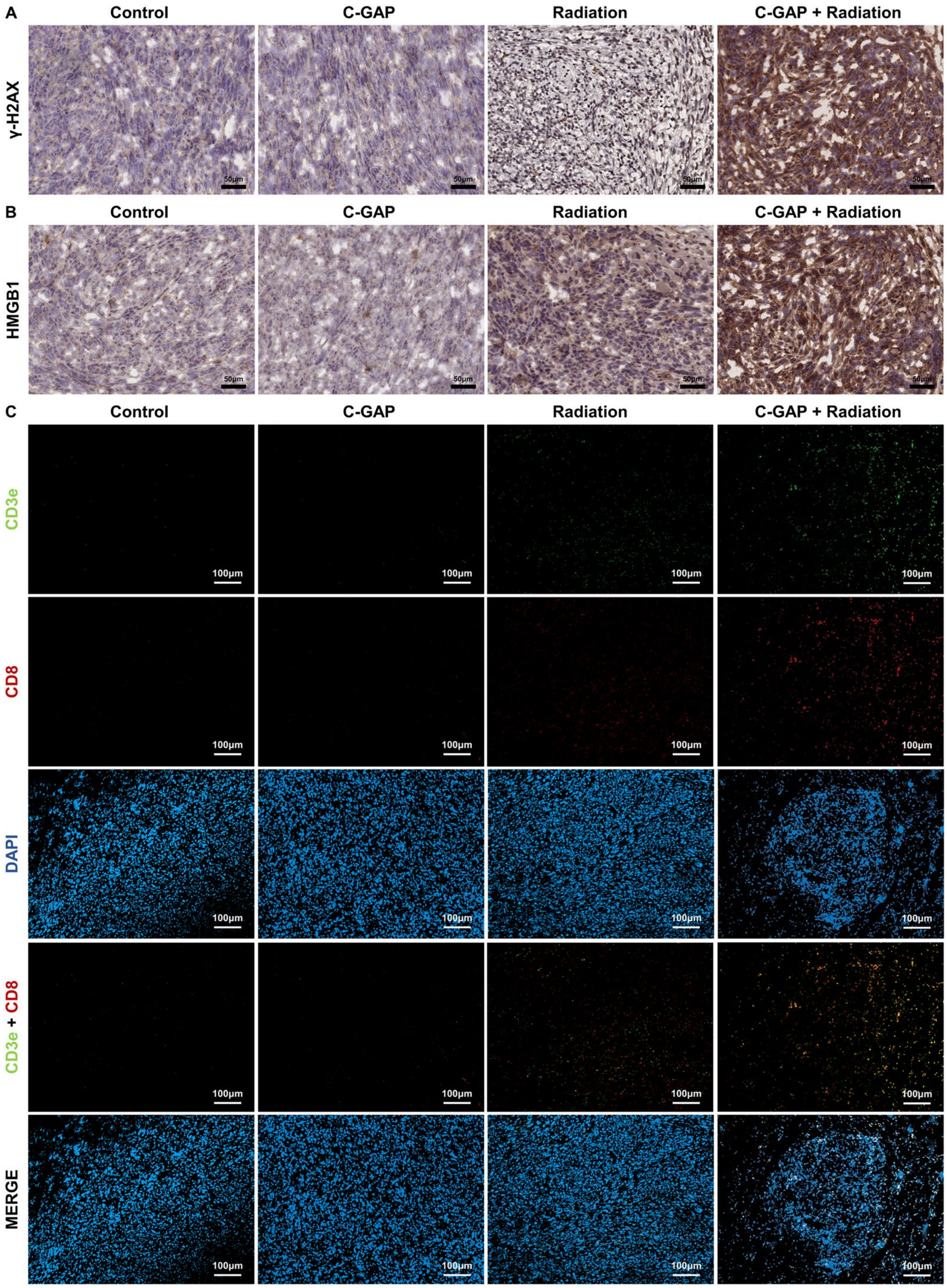

Fig. 7 In Vivo Experiments on C-GAP-Induced ICD in OSCC of C3H Mice. **A** Representative Images of Immunohistochemical Staining for γ-H2AX in Tumor Tissue from C3H Mice in Different Groups (n = 4). **B** Representative Images of Immunohistochemical Staining for HMGB1 in Tumor Tissue from C3H Mice in Different Groups (n = 4). **C** Representative Images of Immunofluorescence Staining for CD3e and CD8 in Tumor Tissue from C3H Mice in Different Groups (n = 4)

of Proliferation T cells slightly decreased (from 3.86% to 1.11%, $p = 0.03 < 0.05$), and there were no statistically significant differences in the proportions of Pre-Exhausted T cells (13.29% vs. 12.62%, $p = 0.48 > 0.05$) and Effector T cells (40.29% vs. 32.97%, $p = 0.23 > 0.05$). The observed results may be attributed to the significant reduction in total tumor cell count in the treatment group compared to the control group. The fate of $CD8^+$ T cells is regulated

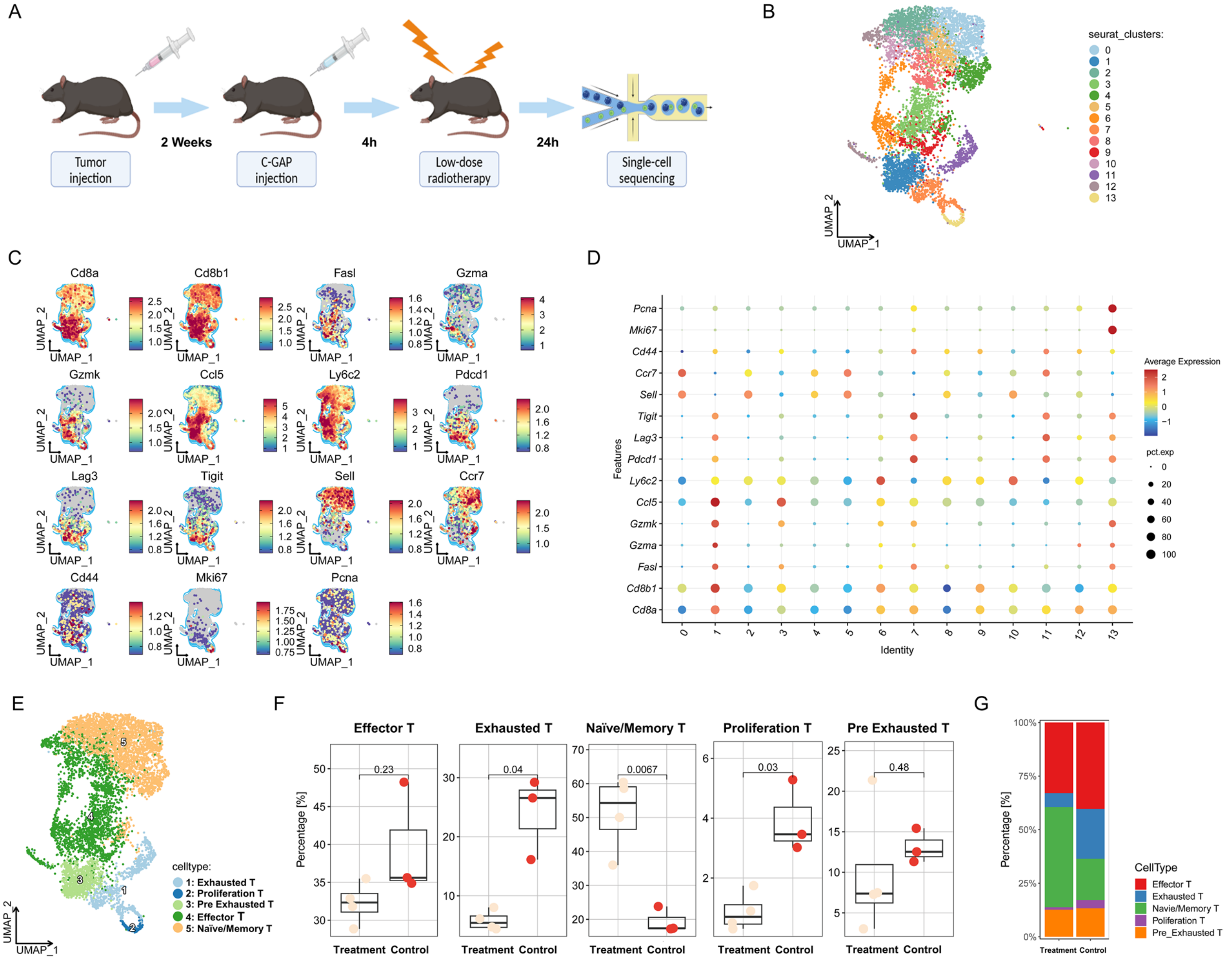

Fig. 8 scRNA-Seq Analysis of CD8$^+$ Cell Distribution and Composition Ratio in OSCC. **A** Diagram of a scRNA-seq Workflow. **B** U-MAP Plots of 5,292 CD8$^+$ T Cells from OSCC Tumors in C3H Mice of the Treatment Group. **C** Feature Plots of Expression Distribution for Selected Cluster-Specific Genes. Expression Levels for Each Cell Are Color-Coded and Overlaid onto the U-MAP Plots. **D** Expression of Selected Cluster-Specific Genes in CD8$^+$ T Cell Subclusters. **E** U-MAP Plots of Five Different Subclusters of CD8$^+$ T Cells from OSCC Tumors in C3H Mice of the Treatment Group. **F-G** Changes in Cell Proportions in Five Different Subclusters of CD8$^+$ T Cells Between the Control Group and the Treatment Group

by tumor antigen [73]. In acute infection, following antigen clearance, most short-lived effector T cells (SLECs) die whereas memory precursor effector cells (MPECs) survive to differentiate into memory CD8 + T cells for long-term protective immunity [74]. Consequently, the reduction in tumor burden after radiotherapy may weaken the persistent antigen signals, thereby terminating the effector state of T cells and promoting the differentiation of memory T cells. The reduction of Effector T cells and Proliferation T cells likely facilitated the partial differentiation into Naive/Memory T cells, consequently leading to a marked increase in the proportion of Naive/Memory T cells within the treatment group.

The results also revealed that the proportion of Exhausted T cells in the Treatment group showed a significant decrease compared to the Control group. This phenomenon may be attributed to low-dose radiation therapy facilitating the release of DNA fragments from tumor cell, which activates the cGAS/STING pathway in tumor. This activation induces type I interferon secretion, promotes dendritic cell (DC) maturation and antigen cross-presentation, ultimately leading to the activation of tumor-specific T cells and consequently reducing the formation of exhausted T cells [75]. Notably, despite these proportional changes, the absolute numbers of all CD8 + T cell subpopulations in the Treatment group demonstrated increases relative to the Control group (The proportions and cell counts of T-cell subpopulations are detailed in Supplementary Table S2). These findings indicate that the upregulation of tumor cell

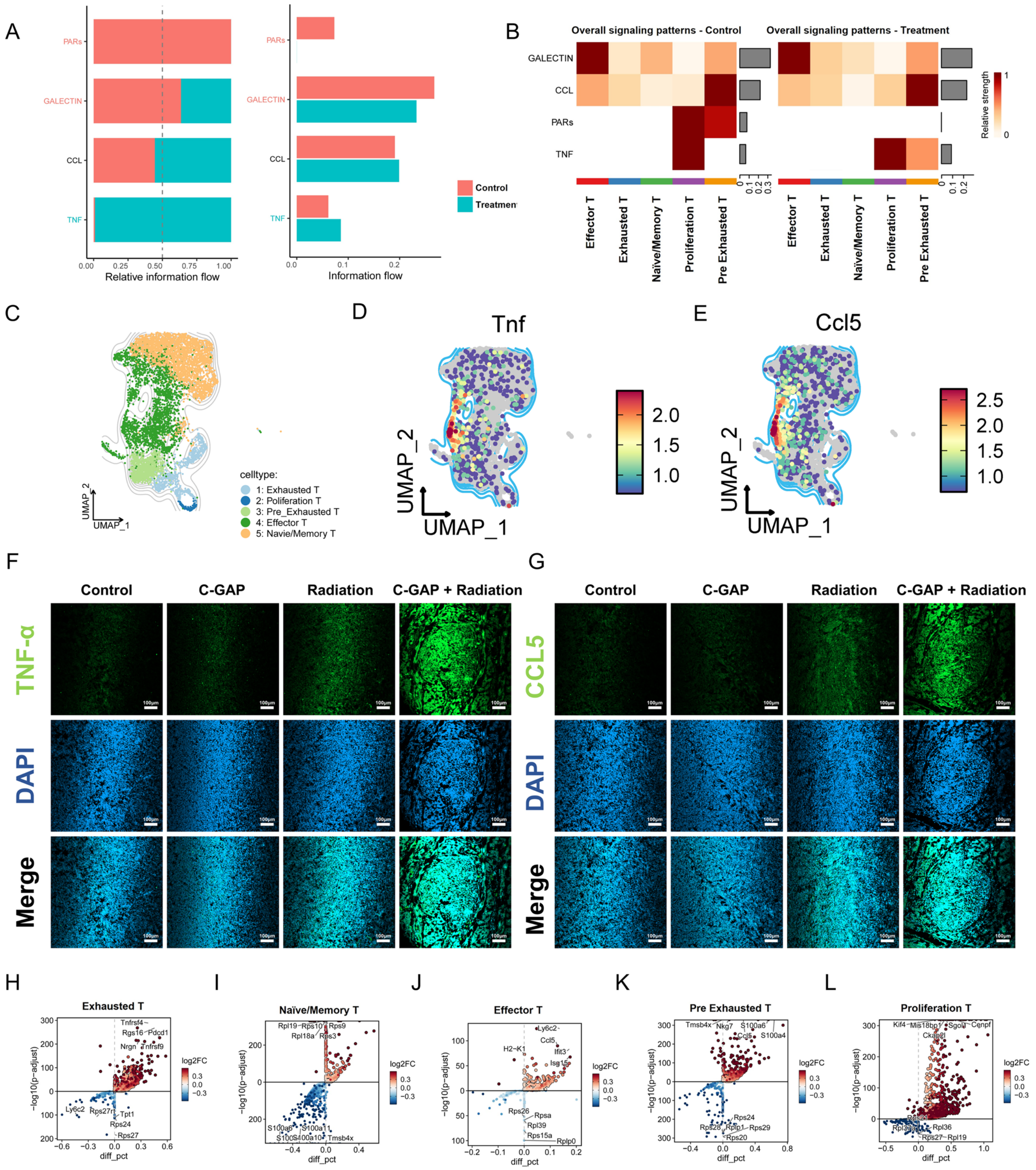

Fig. 9 scRNA-seq Analysis of the Impact of C-GAP on Gene Expression in CD8$^+$ Cells. **A**, **B** Expression of immune-related genes in CD8$^+$ T cell subclusters of the Treatment group. **C** UMAP Plot of different CD8$^+$ T cell subpopulations from Treatment group with lines represent cell density. **D** UMAP plot of the expression and distribution of TNF-α in CD8$^+$T cell subpopulations from Treatment group. **E** UMAP plot of the expression and distribution of CCL5 in CD8$^+$T cell subpopulations from Treatment group. **F-G** Representative Images and Semi-Quantitative Analysis of TNF-α and CCL5 Expression in Mice Tumor Tissue from Different Groups Detected by Immunofluorescence Staining (n = 4). **H–L** Differential Gene Expression Analysis of Five CD8$^+$ T Cell Subclusters within the Treatment Group

immunogenicity in the Treatment group promoted T cell activation, proliferation and regeneration while reducing T cell exhaustion.

Next, we conducted a comparative analysis of the expression of immune-related signaling pathway molecules in CD8$^+$ T cells between the Control and Treatment groups (Fig. 9A, B). The results demonstrated that, compared to the Control group, the expression of CCL and TNF signaling pathway was enhanced in the Treatment group, while the expression of Protease-activated receptors (PARs) and GALECTIN signaling pathway was reduced. Among these, TNF-α acts as a costimulatory signal to promote the activation of CD8$^+$ T cells, thereby enhancing their proliferation and effector functions. It is a hallmark of T cell activation [76]. CCLs are a class of cytokines that exhibit chemotactic effects on immune cells, playing crucial roles in regulating T cell invasion into the tumor microenvironment and mediating T cell migration [77]. In particular, chemokines such as CCL5 [78] and CCL2 [79] have significant regulatory effects on CD8$^+$ T cells. These chemokines enhance antitumor immune responses by attracting CD8$^+$ T cells to infiltrate the tumor area in the tumor microenvironment. In tumors such as ovarian cancer, the expression of CCL5 and CXCL9 correlates specifically with the infiltration of CD8$^+$ T cells [80]. After being activated by TCR-mediated signals, CD8$^+$ T cells can secrete inflammatory cytokines such as TNF-α and chemokines like CCL5, recruiting immune cells and promoting the activation and maturation of DC cells and macrophages, thereby enhancing tumor immunity [81].

Subsequently, we conducted scRNA-seq to analyze the expression of key cytokines TNF-α and CCL5 in CD8 + T cells from the Treatment group. The UMAP results (Fig. 9C–E) demonstrated that TNF-α and CCL5 were predominantly expressed in effector T cells, which represent the primary subpopulation of CD8 + T cells responsible for exerting tumoricidal effects. Additionally, results from in vivo immunofluorescence staining experiments in mice (Fig. 9F, G) showed that, compared to the control group and C-GAP group, the levels of TNF-α and CCL5 infiltration within the tumor immune microenvironment were markedly increased in the Radiation group and the C-GAP + Radiation group. Notably, the highest expression levels of TNF-α and CCL5 were observed in the C-GAP + Radiation group. These findings further confirm the activation of CD8 + T cells by C-GAP-sensitized LDI.

Galectin-9, a member of the galectin family, can induce CD8$^+$ T cell death by binding to TIM-3, thereby promoting tumor progression [82]. Therefore, the downregulation of Galectin expression contributes to maintaining CD8$^+$ T cell activity and enhancing tumor immunity. PARs, members of the class A protein family of G protein-coupled receptors (GPCRs), play a central role in epithelial malignancies [83]. Among them, γδT cells and CD8$^+$ T cells express only PAR1, while CD4$^+$ T cells can express both PAR1 and PAR2. PARs can be activated by tissue factor (TF), promoting angiogenesis in tumor tissues and thus facilitating tumor proliferation and metastasis [84]. The downregulation of PARs helps to inhibit tumor progression. Additionally, GO gene enrichment analysis was performed on the five different subsets of CD8$^+$ T cells in the treatment group (Fig. S5 and Fig. S6). The analysis results showed that immune response-related signaling pathways targeting viruses and interferon-β were significantly upregulated in Effector T cells, suggesting that Effector T cells possess robust killing capabilities. And Fig. 9H–L shows the results of Differential Gene Expression Analysis among the five different T cell subsets in the Treatment group. The above findings demonstrate that C-GAP combined with low-dose irradiation can efficiently activate the tumor-killing capacity of CD8 + T cells.

Conclusion

In summary, based on the concept of homologous targeting, this study successfully synthesized a visual biomimetic nanoparticle, C-GAP. Both in vitro and in vivo experiments verified that C-GAP exhibits excellent biocompatibility and ideal visualization performance. It can precisely target OSCC tumor cells and sensitize low-dose radiotherapy to exert a robust tumor-killing effect. Additionally, C-GAP can promote ICD in OSCC cells and regulate the composition and function of CD8$^+$ T cells, thereby reversing the tumor-induced immunosuppressive microenvironment and demonstrating a significant tumor immune-enhancing effect. The low-dose radiotherapy therapy based on C-GAP can enhance tumor immunity and holds potential as a novel and promising treatment approach to improve the prognosis of OSCC.

Abbreviations

OSCC	Oral squamous cell carcinoma
ICD	Immunogenic cell death
N-GQDs	Nitrogen-doped Graphene Quantum Dots
AuNP	Au nanoparticles
ROS	Reactive oxygen species
DAMPs	Damage-associated molecular patterns
PRRs	Pattern recognition receptors
CAMs	Cell adhesion molecules
scRNA-seq	Single-cell RNA sequencing

C-GAP	Cell membrane coated-nitrogen-doped Graphene quantum dots combined with Au nanoparticles
DCD	Dicyandiamide
CA	Citric acid
AFM	Atomic force microscopy
EDS	Energy dispersive X-ray spectroscopy
TEM	Transmission electron microscopy
XPS	X-ray photoelectron spectroscopy
RER	Rough Endoplasmic Reticulum
ASS	Autophagolysosome
GPCRs	G protein-coupled receptors
GO	Gene Ontology

Supplementary Information

The online version contains supplementary material available at https://doi.org/10.1186/s12951-025-03281-6.

Supplementary Material 1.

Acknowledgements

Not applicable.

Author contributions

Conceptualization, data collecting, and original draft writing: WZ (Weijie Zhuang), JW and KP; Methodology: WZ (Weijie Zhuang), LL, SL, JH, FS; Original draft review, polishing and editing: WZ (Wei Zhao) and DY; Project administration and funding acquisition: DY. All authors have read and agreed to the published version of the manuscript.

Funding

This work was financially supported by the National Natural Science Foundation of China [grant number 82373255] and the Natural Science Foundation of Guangdong Province [grant number 2024A1515012918].

Availability of data and materials

The datasets used and analyzed during the current study are available from the corresponding author on reasonable request.

Declarations

Ethics approval and consent to participate

All animal experiment procedures were conducted in strict accordance with relevant laws and regulations, and approved by the Institutional Animal Care and Use Committee (IACUC) of Sun Yat-Sen University (Reference: SYSU-IACUC-2024–001533).

Consent for publication

Not applicable.

Competing interests

The authors declare no competing interests.

Author details

[1]Hospital of Stomatology, Guanghua School of Stomatology, Sun Yat-sen University, Guangzhou 510055, China. [2]Guangdong Provincial Key Laboratory of Stomatology, Sun Yat-sen University, Guangzhou 510050, China. [3]Department of Stomatology, The Third People's Hospital of Chengdu, Sichuan, China.

Received: 8 January 2025 Accepted: 26 February 2025

References

1. Liu J, Jiang X, Zou A, Mai Z, Huang Z, Sun L, et al. circIGHG-induced epithelial-to-mesenchymal transition promotes oral squamous cell carcinoma progression via miR-142-5p/IGF2BP3 signaling. Cancer Res. 2021;81:344–55.
2. Bray F, Ferlay J, Soerjomataram I, Siegel RL, Torre LA, Jemal A. Global cancer statistics 2018: GLOBOCAN estimates of incidence and mortality worldwide for 36 cancers in 185 countries. CA Cancer J Clin. 2018;68:394–424.
3. Zhang Y, Zhang Z. The history and advances in cancer immunotherapy: understanding the characteristics of tumor-infiltrating immune cells and their therapeutic implications. Cell Mol Immunol. 2020;17:807–21.
4. Le Meitour Y, Foy J-P, Guinand M, Michon L, Karabajakian A, Fayette J, et al. Uncovering immune checkpoint heterogeneity in oral squamous cell carcinoma using single cell RNA-sequencing data highlights three subgroups of patients with distinct immune phenotypes. Oral Oncol. 2024;149: 106680.
5. Diao P, Jiang Y, Li Y, Wu X, Li J, Zhou C, et al. Immune landscape and subtypes in primary resectable oral squamous cell carcinoma: prognostic significance and predictive of therapeutic response. J Immunother Cancer. 2021;9: e002434.
6. Shi Y, Xie T, Wang B, Wang R, Cai Y, Yuan B, et al. Mutant p53 drives an immune cold tumor immune microenvironment in oral squamous cell carcinoma. Commun Biol. 2022;5:757.
7. Liu Y-T, Sun Z-J. Turning cold tumors into hot tumors by improving T-cell infiltration. Theranostics. 2021;11:5365–86.
8. Huang SH, Hahn E, Chiosea SI, Xu Z-Y, Li J-S, Shen L, et al. The role of adjuvant (chemo-)radiotherapy in oral cancers in the contemporary era. Oral Oncol. 2020;102: 104563.
9. Falcke SE, Rühle PF, Deloch L, Fietkau R, Frey B, Gaipl US. Clinically relevant radiation exposure differentially impacts forms of cell death in human cells of the innate and adaptive immune system. Int J Mol Sci. 2018;19:3574.
10. Chen G, Li Y, He Y, Zeng B, Yi C, Wang C, et al. Upregulation of circular RNA circATRNL1 to sensitize oral squamous cell carcinoma to irradiation. Mol Ther Nucleic Acids. 2020;19:961–73.
11. Liu T, Pei P, Shen W, Hu L, Yang K. Radiation-induced immunogenic cell death for cancer radioimmunotherapy. Small Methods. 2023;7: e2201401.
12. Galluzzi L, Guilbaud E, Schmidt D, Kroemer G, Marincola FM. Targeting immunogenic cell stress and death for cancer therapy. Nat Rev Drug Discov. 2024;23:445–60.
13. Jarosz-Biej M, Smolarczyk R, Cichoń T, Kułach N. Tumor microenvironment as a "game changer" in cancer radiotherapy. Int J Mol Sci. 2019;20:3212.
14. Wang J, Ma J, Xie F, Miao F, lv L, Huang Y, et al. Immunogenic cell death-based cancer vaccines: promising prospect in cancer therapy. Front Immunol. 2024;15:1389173.
15. Galluzzi L, Aryankalayil MJ, Coleman CN, Formenti SC. Emerging evidence for adapting radiotherapy to immunotherapy. Nat Rev Clin Oncol. 2023;20:543–57.
16. Wang H, Jiang H, Van De Gucht M, De Ridder M. Hypoxic radioresistance: can ROS be the key to overcome it? Cancers. 2019;11:112.
17. Hellevik T, Martinez-Zubiaurre I. Radiotherapy and the tumor stroma: the importance of dose and fractionation. Front Oncol. 2014;4:1.
18. Ochoa de Olza M, Bourhis J, Irving M, Coukos G, Herrera FG. High versus low dose irradiation for tumor immune reprogramming. Curr Opin Biotechnol. 2020;65:268–83.
19. Herrera FG, Romero P, Coukos G. Lighting up the tumor fire with low-dose irradiation. Trends Immunol. 2022;43(3):173–9.
20. Luo K, Guo W, Yu Y, Xu S, Zhou M, Xiang K, et al. Reduction-sensitive platinum (IV)-prodrug nano-sensitizer with an ultra-high drug loading for efficient chemo-radiotherapy of Pt-resistant cervical cancer in vivo. J Controlled Release. 2020;326:25–37.
21. Wang Z, Ren X, Wang D, Guan L, Li X, Zhao Y, et al. Novel strategies for tumor radiosensitization mediated by multifunctional gold-based nanomaterials. Biomater Sci. 2023;11:1116–36.
22. Liu J, Wu J, Chen T, Yang B, Liu X, Xi J, et al. Enhancing X-ray sensitization with multifunctional nanoparticles. Small. 2024;20:2400954.
23. Qi H, Li Y, Geng Y, Wan X, Cai X. Nanoparticle-mediated immunogenic cell death for cancer immunotherapy. Int J Pharm. 2024;656: 124045.
24. Peng J, Li S, Ti H. Sensitize tumor immunotherapy: immunogenic cell death inducing nanosystems. Int J Nanomedicine. 2024;19:5895–930.
25. Henna TK, Pramod K. Graphene quantum dots redefine nanobiomedicine. Mater Sci Eng C. 2020;110: 110651.

26. Zhang X, Wei C, Li Y, Yu D. Shining luminescent graphene quantum dots: Synthesis, physicochemical properties, and biomedical applications. TrAC Trends Anal Chem. 2019;116:109–21.
27. Qin X, Zhan Z, Zhang R, Chu K, Whitworth Z, Ding Z. Nitrogen- and sulfur-doped graphene quantum dots for chemiluminescence. Nanoscale. 2023;15:3864–71.
28. Iannazzo D, Pistone A, Salamò M, Galvagno S, Romeo R, Giofré SV, et al. Graphene quantum dots for cancer targeted drug delivery. Int J Pharm. 2017;518:185–92.
29. Kuo W-S, Chen H-H, Chen S-Y, Chang C-Y, Chen P-C, Hou Y-I, et al. Graphene quantum dots with nitrogen-doped content dependence for highly efficient dual-modality photodynamic antimicrobial therapy and bioimaging. Biomaterials. 2017;120:185–94.
30. Wu T, Wang X, Cheng J, Liang X, Li Y, Chen M, et al. Nitrogen-doped graphene quantum dots induce ferroptosis through disrupting calcium homeostasis in microglia. Part Fibre Toxicol. 2022;19:22.
31. Wu T, Liang X, Liu X, Li Y, Wang Y, Kong L, et al. Induction of ferroptosis in response to graphene quantum dots through mitochondrial oxidative stress in microglia. Part Fibre Toxicol. 2020;17:30.
32. Wang H, Mu X, He H, Zhang X-D. Cancer radiosensitizers. Trends Pharmacol Sci. 2018;39:24–48.
33. Wang W, Liu J, Feng W, Du S, Ge R, Li J, et al. Targeting mitochondria with Au-Ag@Polydopamine nanoparticles for papillary thyroid cancer therapy. Biomater Sci. 2019;7:1052–63.
34. Liang R, Xie J, Li J, Wang K, Liu L, Gao Y, et al. Liposomes-coated gold nanocages with antigens and adjuvants targeted delivery to dendritic cells for enhancing antitumor immune response. Biomaterials. 2017;149:41–50.
35. Qin X, Yang C, Xu H, Zhang R, Zhang D, Tu J, et al. Cell-derived biogenetic gold nanoparticles for sensitizing radiotherapy and boosting immune response against cancer. Small. 2021;17:2103984.
36. Chen Y, Yang J, Fu S, Wu J. Gold nanoparticles as radiosensitizers in cancer radiotherapy. Int J Nanomedicine. 2020;15:9407–30.
37. Fan D, Cao Y, Cao M, Wang Y, Cao Y, Gong T. Nanomedicine in cancer therapy. Signal Transduct Target Ther. 2023. https://doi.org/10.1038/s41392-023-01536-y.
38. Zeng Y, Li S, Zhang S, Wang L, Yuan H, Hu F. Cell membrane coated-nanoparticles for cancer immunotherapy. Acta Pharm Sin B. 2022;12:3233–54.
39. Fang RH, Hu CMJ, Luk BT, Gao W, Copp JA, Tai Y, et al. Cancer cell membrane-coated nanoparticles for anticancer vaccination and drug delivery. Nano Lett. 2014;14:2181–8.
40. Xia J, Cheng Y, Zhang H, Li R, Hu Y, Liu B. The role of adhesions between homologous cancer cells in tumor progression and targeted therapy. Expert Rev Anticancer Ther. 2017;17:517–26.
41. Gong L, Zhang Y, Zhao J, Zhang Y, Tu K, Jiao L, et al. All-in-one biomimetic nanoplatform based on hollow polydopamine nanoparticles for synergistically enhanced radiotherapy of colon cancer. Small. 2022;18:2107656.
42. Pereira-Silva M, Santos AC, Conde J, Hoskins C, Concheiro A, Alvarez-Lorenzo C, et al. Biomimetic cancer cell membrane-coated nanosystems as next-generation cancer therapies. Expert Opin Drug Deliv. 2020;17:1515–8.
43. Pan W-L, Tan Y, Meng W, Huang N-H, Zhao Y-B, Yu Z-Q, et al. Microenvironment-driven sequential ferroptosis, photodynamic therapy, and chemotherapy for targeted breast cancer therapy by a cancer-cell-membrane-coated nanoscale metal-organic framework. Biomaterials. 2022;283: 121449.
44. Wu Q, Tong L, Zou Z, Li Y, An J, Shen W, et al. Herceptin-functionalized SK-BR-3 cell membrane-wrapped paclitaxel nanocrystals for enhancing the targeted therapy effect of HER2-positive breast cancer. Mater Des. 2022;219: 110818.
45. Gan J, Du G, He C, Jiang M, Mou X, Xue J, et al. Tumor cell membrane enveloped aluminum phosphate nanoparticles for enhanced cancer vaccination. J Control Release Off J Control Release Soc. 2020;326:297–309.
46. Jiang Y, Krishnan N, Zhou J, Chekuri S, Wei X, Kroll AV, et al. Engineered cell-membrane-coated nanoparticles directly present tumor antigens to promote anticancer immunity. Adv Mater Deerfield Beach Fla. 2020;32: e2001808.
47. Ran P, Song J, Mo F, Wu J, Liu P, Fu Y. Nitrogen-doped graphene quantum dots coated with gold nanoparticles for electrochemiluminescent glucose detection using enzymatically generated hydrogen peroxide as a quencher. Mikrochim Acta. 2019;186:276.
48. Kaur M, Kaur M, Sharma VK. Nitrogen-doped graphene and graphene quantum dots: a review onsynthesis and applications in energy, sensors and environment. Adv Colloid Interface Sci. 2018;259:44–64.
49. Wu Z, Xia W, Ou L, Zheng L, Hou B, Pan T, et al. Utilization of nitrogen-doped graphene quantum dots to neutralize ROS and modulate intracellular antioxidant pathways to improve dry eye disease therapy. Int J Nanomedicine. 2024;19:2691–708.
50. Mahmoud AM, Mahnashi MH, Alkahtani SA, El-Wekil MM. Nitrogen and sulfur co-doped graphene quantum dots/nanocellulose nanohybrid for electrochemical sensing of anti-schizophrenic drug olanzapine in pharmaceuticals and human biological fluids. Int J Biol Macromol. 2020;165:2030–7.
51. Ju J, Chen W. In situ growth of surfactant-free gold nanoparticles on nitrogen-doped graphene quantum dots for electrochemical detection of hydrogen peroxide in biological environments. Anal Chem. 2015;87:1903–10.
52. Ding H, Yu S-B, Wei J-S, Xiong H-M. Full-color light-emitting carbon dots with a surface-state-controlled luminescence mechanism. ACS Nano. 2016;10:484–91.
53. Ferrari AC, Basko DM. Raman spectroscopy as a versatile tool for studying the properties of graphene. Nat Nanotechnol. 2013;8:235–46.
54. Dervishi E, Ji Z, Htoon H, Sykora M, Doorn SK. Raman spectroscopy of bottom-up synthesized graphene quantum dots: size and structure dependence. Nanoscale. 2019;11:16571–81.
55. Pathak PK, Kumar A, Prasad BB. Functionalized nitrogen doped graphene quantum dots and bimetallic Au/Ag core-shell decorated imprinted polymer for electrochemical sensing of anticancerous hydroxyurea. Biosens Bioelectron. 2019;127:10–8.
56. Özönder Ş, Ünlü C, Güleryüz C, Trabzon L. Doped graphene quantum dots UV-vis absorption spectrum: a high-throughput TDDFT study. ACS Omega. 2023;8:2112–8.
57. Xu A, Wang G, Li Y, Dong H, Yang S, He P, et al. Carbon-based quantum dots with solid-state photoluminescent: mechanism, implementation, and application. Small Weinh Bergstr Ger. 2020;16: e2004621.
58. Chung S, Revia RA, Zhang M. Graphene quantum dots and their applications in bioimaging, biosensing, and therapy. Adv Mater Deerfield Beach Fla. 2021;33: e1904362.
59. Lu H, Li W, Dong H, Wei M. Graphene quantum dots for optical bioimaging. Small Weinh Bergstr Ger. 2019;15: e1902136.
60. Khodadadei F, Safarian S, Ghanbari N. Methotrexate-loaded nitrogen-doped graphene quantum dots nanocarriers as an efficient anticancer drug delivery system. Mater Sci Eng C. 2017;79:280–5.
61. Tabaraki R, Nateghi A. Nitrogen-doped graphene quantum dots: "Turn-off" fluorescent probe for detection of Ag(+) ions. J Fluoresc. 2016;26:297–305.
62. Algarra M, Moreno V, Lázaro-Martínez JM, Rodríguez-Castellón E, Soto J, Morales J, et al. Insights into the formation of N doped 3D-graphene quantum dots. Spectroscopic and computational approach. J Colloid Interface Sci. 2020;561:678–86.
63. Hu C, Liu Y, Yang Y, Cui J, Huang Z, Wang Y, et al. One-step preparation of nitrogen-doped graphene quantum dots from oxidized debris of graphene oxide. J Mater Chem B. 2012;1:39–42.
64. Liang J, Liu Y, Si Z, Wei G, Weng D, Kang F. Graphene quantum dots piecing together into graphene on nano Au for overall water splitting. Carbon. 2021;178:265–72.
65. Ţucureanu V, Matei A, Avram AM. FTIR spectroscopy for carbon family study. Crit Rev Anal Chem. 2016;46:502–20.
66. Fang RH, Gao W, Zhang L. Targeting drugs to tumours using cell membrane-coated nanoparticles. Nat Rev Clin Oncol. 2023;20:33–48.
67. Guo Q, Wang S, Xu R, Tang Y, Xia X. Cancer cell membrane-coated nanoparticles: a promising anti-tumor bionic platform. RSC Adv. 2024;14:10608–37.
68. Liu Y, Wang Y, Sun S, Chen Z, Xiang S, Ding Z, et al. Understanding the versatile roles and applications of EpCAM in cancers: from bench to bedside. Exp Hematol Oncol. 2022;11:97.
69. Patel RB, Hernandez R, Carlson P, Grudinski J, Bates AM, Jagodinsky JC, et al. Low-dose targeted radionuclide therapy renders immunologically "cold" tumors responsive to immune checkpoint blockade. Sci Transl Med. 2021;13:eabb3631.
70. Wang Y, Chen J, Duan R, Gu R, Wang W, Wu J, et al. High-Z-sensitized radiotherapy synergizes with the intervention of the pentose

phosphate pathway for in situ tumor vaccination. Adv Mater Deerfield Beach Fla. 2022;34: e2109726.

71. Xu P, Ma J, Zhou Y, Gu Y, Cheng X, Wang Y, et al. Radiotherapy-triggered in situ tumor vaccination boosts checkpoint blockaded immune response via antigen-capturing nanoadjuvants. ACS Nano. 2024;18:1022–40.
72. Zhao C, Song X, Liu Y, Fu Y, Ye L, Wang N, et al. Synthesis of graphene quantum dots and their applications in drug delivery. J Nanobiotechnology. 2020;18:142.
73. Chen Y, Yu D, Qian H, Shi Y, Tao Z. CD8+ T cell-based cancer immunotherapy. J Transl Med. 2024;22:394.
74. Dolina JS, Van Braeckel-Budimir N, Thomas GD, Salek-Ardakani S. CD8+ T Cell exhaustion in cancer. Front Immunol. 2021. https://doi.org/10.3389/fimmu.2021.715234.
75. Wang H, Yao Z, Kang K, Zhou L, Xiu W, Sun J, et al. Preclinical study and phase II trial of adapting low-dose radiotherapy to immunotherapy in small cell lung cancer. Med N Y N. 2024;5:1237-1254.e9.
76. Kammertoens T, Friese C, Arina A, Idel C, Briesemeister D, Rothe M, et al. Tumour ischaemia by interferon-γ resembles physiological blood vessel regression. Nature. 2017;545:98.
77. Mempel TR, Lill JK, Altenburger LM. How chemokines organize the tumour microenvironment. Nat Rev Cancer. 2024;24:28–50.
78. Jacobs C, Shah S, Lu W-C, Ray H, Wang J, Hockaden N, et al. HSF1 inhibits antitumor immune activity in breast cancer by suppressing CCL5 to block CD8+ T-cell recruitment. Cancer Res. 2024;84:276–90.
79. Shi Z, Yu P, Lin W-J, Chen S, Hu X, Chen S, et al. Microglia drive transient insult-induced brain injury by chemotactic recruitment of CD8+ T lymphocytes. Neuron. 2023;111:696-710.e9.
80. Dangaj D, Bruand M, Grimm AJ, Ronet C, Barras D, Duttagupta PA, et al. Cooperation between constitutive and inducible chemokines enables T cell engraftment and immune attack in solid tumors. Cancer Cell. 2019;35:885-900.e10.
81. Hoekstra ME, Slagter M, Urbanus J, Toebes M, Slingerland N, de Rink I, et al. Distinct spatiotemporal dynamics of CD8+ T cell-derived cytokines in the tumor microenvironment. Cancer Cell. 2024;42:157-167.e9.
82. Yang R, Sun L, Li C-F, Wang Y-H, Yao J, Li H, et al. Galectin-9 interacts with PD-1 and TIM-3 to regulate T cell death and is a target for cancer immunotherapy. Nat Commun. 2021;12:832.
83. Bar-Shavit R, Maoz M, Kancharla A, Jaber M, Agranovich D, Grisaru-Granovsky S, et al. Chapter 16 - Protease-activated receptors (PARs) in cancer: Novel biased signaling and targets for therapy. In: K. Shukla A, editor. Methods Cell Biol 2016, p. 341–58.
84. Tieken C, Versteeg HH. Anticoagulants versus cancer. Thromb Res. 2016;140(Suppl 1):S148-153.

Publisher's Note